Materials Science and Engineering, 33 (2001) 51–107

R Reports: A Review Journal

www.elsevier.com/locate/mser

Ion implantation into GaN

S.O. Kucheyev[a,*], J.S. Williams[a], S.J. Pearton[b]

[a]Department of Electronic Materials Engineering, Research School of Physical Sciences and Engineering, The Australian National University, Canberra, ACT 0200, Australia

[b]Department of Materials Science and Engineering, University of Florida, Gainesville, FL 32611, USA

Accepted 18 January 2001

Abstract

The current status of ion beam processing of GaN is reviewed. In particular, we discuss the following aspects of ion implantation into GaN: (i) damage build-up and amorphization, (ii) preferential surface disordering and loss of nitrogen during ion bombardment, (iii) ion-beam-induced porosity of amorphous GaN due to material dissociation, (iv) anomalous surface erosion during ion bombardment at elevated temperatures, (v) the effect of implantation disorder on mechanical properties, (vi) current progress on annealing of implantation disorder, (vii) electrical and optical doping, and (viii) electrical isolation. Emphasis is given to current problems which may hinder a successful application of ion implantation in the fabrication of GaN-based devices. © 2001 Elsevier Science B.V. All rights reserved.

Keywords: GaN; Ion implantation; Implantation disorder; Annealing

1. Introduction

For much of the past decade, GaN has been a subject of extensive research due to very important technological applications of this material. As is well documented in the literature [1], current applications of GaN include light-emitting diodes (LEDs), laser diodes, UV detectors, and microwave power and ultra-high power switches. In the fabrication of such GaN-based devices, ion bombardment represents a very attractive tool for several technological steps, such as electrical and optical selective-area doping, dry etching, electrical isolation, quantum well intermixing, and ion-cut. It is well-known that a successful application of ion implantation depends on understanding the production and annealing of radiation damage. Thus, detailed studies of ion implantation damage in GaN are not only important for investigating fundamental defect processes in solids under ion bombardment but are also essential for the fast developing GaN industry.

Up to now, several outstanding reviews have appeared in the literature addressing various aspects of ion implantation into GaN [1–4]. However, very recently, the field of ion implantation into GaN has matured considerably. This review mainly concentrates on the recent progress made in the understanding of ion beam processes in GaN, which has not been reviewed previously. Sections 2–4 treat the structural characteristics of GaN exposed to ion bombardment. The mechanical properties of as-grown and ion implanted GaN are discussed in Section 5. In Section 6, we briefly discuss the

* Corresponding author. Tel.: +61-2-61250464; fax: +61-2-61250511.
E-mail address: sergei.kucheyev@anu.edu.au (S.O. Kucheyev).

0927-796X/01/$ – see front matter © 2001 Elsevier Science B.V. All rights reserved.
PII: S0927-796X(01)00028-6

current progress on the annealing of implantation damage. Sections 7 and 8 address the optical and electrical characteristics, respectively. Applications of ion implantation in the fabrication of GaN-based electronic devices are discussed in Section 9. Finally, in Section 10, we summarize the current problems of ion beam processing of GaN which may limit the applications of ion implantation for the fabrication of GaN-based devices.

A comment should be made about what is not included in detail in this review. We only briefly discuss the lattice sites of dopants implanted into GaN, studies of specific defect levels by deep level transient spectroscopy (DLTS), and studies of lattice disorder produced by dry etching (a recent review on this topic can be found in [6]). Some of these studies have been reviewed in [1,5]. For the same reason, we omit the discussion of rare-earth doping of GaN by ion implantation as well as the effects of hydrogen implanted into GaN (see [1,5] for details on these topics). In addition, potential applications of ion implantation for ion-cut and quantum well intermixing in GaN are also only briefly mentioned here due to the lack of published literature on these subjects.

2. Damage build-up

Lattice disorder is always a concomitant effect of ion bombardment. Undesirable damage produced by an ion beam is, in fact, the main problem for satisfactory electrical and optical doping made by ion implantation. Dry etching is also always accompanied by undesirable damage introduced into near-surface layers. Therefore, studies of implantation disorder and its consequences are necessary for a successful application of ion implantation in device fabrication. In this section, we discuss damage build-up in wurtzite GaN under ion bombardment.

2.1. Atomic displacements versus stable lattice damage

Given the current understanding of ion–solid interactions (see, for example, [7]), an energetic ion penetrating through a GaN crystal generates a collision cascade which consists of vacancies in the gallium and nitrogen sublattices (V_{Ga} and V_N), gallium and nitrogen interstitials (Ga_i and N_i) [1], and, presumably, an amorphous zone in the cascade core in the case of heavy ions.[1] Such a completely disordered or amorphous zone is expected to form (but may not be stable) when the damage level (and/or the energy deposited) in the collision (sub)cascade volume exceeds some threshold value [8–10].

Ion ranges and atomic displacements produced in GaN by ion bombardment can be calculated using, for example, the TRIM code [11], a Monte Carlo computer simulation program. Other methods often used to calculate the profiles of implanted species and atoms displaced involve analytical calculations such as developed by Lindhard, Scharf, and Schiott (often called the LSS theory [7]) and an approach based on the Boltzmann transport equation [12]. For example, Fig. 1 shows profiles of vacancies produced in GaN by implantation with 40 keV ^{12}C, 100 keV ^{197}Au, and 300 keV ^{197}Au ions, as calculated using the TRIM code [11]. It is seen from this figure that ion implantation produces Gaussian-like (uni-modal) profiles of atomic displacements. The thickness of the layer modified by ion bombardment as well as the number of atomic displacements generated depends on ion mass and energy, as illustrated in Fig. 1.

Such theoretical calculations of atomic displacements take into account only ballistic processes and completely neglect dynamic annealing (i.e. defect interaction processes). However, ion-

[1] Here, we do not distinguish between interstitials of different symmetry.

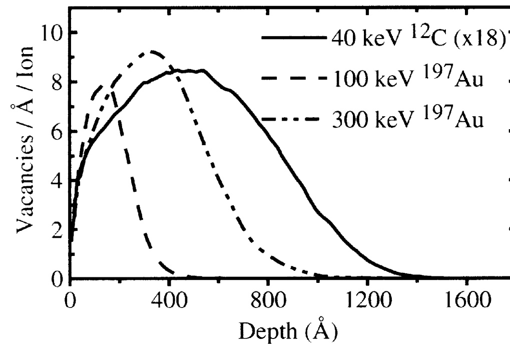

Fig. 1. The profiles of the total number of vacancies produced in GaN by 40 keV ^{12}C, 100 keV ^{197}Au, and 300 keV ^{197}Au ions, as calculated using the TRIM code.

generated simple point defects (V_{Ga}, V_N, Ga_i, and N_i), which survive after quenching of collision cascades, may migrate through the lattice and experience annihilation and cluster formation. As a result, damage–depth profiles in GaN experimentally measured after ion bombardment may depart from predictions based only on collisional processes.

It is well-known that complex dynamic annealing processes in solids under ion bombardment are highly dependent on implant conditions such as ion mass, energy, dose, substrate temperature, and beam flux (see for example [4]). In contrast to our ability to calculate atomic displacements in solids, stable lattice disorder produced by ion bombardment is usually difficult to predict. Experimental studies are essential to both determine and understand the effects of implant conditions on implantation disorder. Such studies are very important because lattice disorder strongly affects device performance.

The structural characteristics of semiconductors exposed to ion bombardment are usually studied by Rutherford backscattering/channeling (RBS/C) spectrometry, (cross-sectional) transmission electron microscopy (XTEM), and X-ray diffraction (XRD). RBS/C is a very powerful, depth-sensitive technique often used to monitor the gross level of lattice disorder produced by ion bombardment [13]. XTEM is currently one of the most powerful techniques used to identify the nature of implantation-produced defects. In addition, XRD is often used to study lattice distortions (stress) produced by ion bombardment.

The structural characteristics of ion bombarded GaN have been studied by several groups [4–39], as summarized in Table 1. It is seen from this table that damage build-up (i.e. lattice disorder as a function of ion dose) has been studied using RBS/C, XTEM, and/or XRD by several groups for ions of different masses (from ^{1}H to ^{197}Au), for different ion energies, and at different implantation temperatures. However, few reports [26,33,35] have been published on the flux effect (i.e. implantation to the same doses with different values of beam flux (dose rate)). Below, we discuss the main features of damage build-up in GaN and the current understanding of dynamic annealing processes in this material. We will also give a brief comparison of damage processes in GaN with those in Si and GaAs.

2.2. Dynamic annealing

The first study of damage accumulation in GaN reported by Tan et al. [14,15] revealed that GaN exhibits very efficient dynamic annealing during bombardment with 90 keV Si ions at liquid nitrogen temperature (LN_2). This conclusion directly follows from the fact that the amount of lattice

Table 1
A summary of damage build-up studies (structural characteristics)

Ion	Energy (keV)	Implantation temperature (°C)	Ion dose (10^{14} cm^{-2})	Analysis	References
Si	90	−196	0.5–400	RBS/C, XTEM	[14,15,21]
Te	350	−196, 20, 200	10	RBS/C	[21]
Zn	200	20	0.5, 50	XTEM, XRD	[16]
Si	160	550	10	RBS/C, XTEM	[17]
Mg	120	20, 550	1, 5, 10	RBS/C	[17]
Ca	180	−196	0.05–60	RBS, XTEM, XRD	[18,22,27,31]
Ar	180	−196	0.05–60	RBS/C, XTEM, XRD	[18,22]
Mg	90	25, 300, 550	1–50	RBS/C	[26,27]
Si	100	−196, 20, 700	0.01–70	RBS/C	[20]
Mg	80	−196, 20, 700	0.01–70	RBS/C	[20]
Mg	150	20	0.5	XRD	[23]
Be	200	20	5	XRD	[23]
O	600[a]	−83, −63	0.5–500	RBS/C	[24]
Au	1000[a]	−93, 20	0.4–50	RBS/C	[29]
^{2}H	50	20	10–1000	RBS/C	[25]
^{1}H	10	−196, 20	1–2000	RBS/C	[39]
C	40	−196, 20	10–3000	RBS/C, XTEM	[30,33]
Au	100	−196, 20	0.5–10	RBS/C, XTEM	[33]
Au	300	−196, 20, 100, 300, 550	0.3–30	RBS/C, XTEM	[28,30,33,35,37,39]
Au	2000	−196, 20	4–100	RBS/C, XTEM, AFM	[32,35,36,39]

[a] Implantation 60° off surface normal.

disorder measured experimentally is much less than that predicted by ballistic calculations (such as the TRIM code [11]), which take into account only collisional processes and neglect defect diffusion and annihilation. Further studies of damage processes in GaN [16–37,39] have confirmed the presence of very efficient dynamic annealing in GaN under a wide range of implant conditions (see Table 1). These studies [16–37,39] have also revealed a number of other interesting features of damage build-up in GaN under ion bombardment, which will be discussed below.

First of all, strong dynamic annealing in GaN results in a somewhat unexpected damage build-up behavior with increasing ion dose. For example, shown in Fig. 2 are RBS/C spectra illustrating damage accumulation in GaN with dose for 300 keV Au ions implanted at LN_2 with a beam flux of 3.1×10^{12} cm^{-2} s^{-1} (Fig. 2(a)) and at room temperature (RT) with a beam flux of 4.4×10^{12} cm^{-2} s^{-1} (Fig. 2(b)). A comparison of Fig. 2(a) and (b) reveals quite different damage build-up behavior with increasing dose of 300 keV Au ions for LN_2 and RT bombardment regimes. Indeed, for LN_2 irradiation, for doses up to $\sim 2 \times 10^{14}$ cm^{-2}, Fig. 2(a) shows accumulation of damage preferentially at the GaN surface, away from the maximum of the nuclear energy loss profile (see Fig. 1). Then, in a narrow dose range from $\sim 2 \times 10^{14}$ to $\sim 3 \times 10^{14}$ cm^{-2}, damage in the GaN bulk region ($\sim$500 Å from the GaN surface) exhibits a very rapid increase from a very low level to complete disordering (i.e. to amorphization), as indicated by the RBS/C yield reaching the random level. In this latter case, amorphization has also been confirmed by XTEM [33]. This rapid build-up of disorder results in a strong sigmodality of the damage–dose function (see Fig. 3), which is characteristic for the case of strong dynamic annealing and nucleation-limited amorphization [33]. In contrast to LN_2, bombardment at RT does not result in such a fast growth of damage in the bulk region with increasing ion dose (see Fig. 2(b)). Instead, damage in the bulk region saturates below the random level, and amorphization proceeds layer-by-layer from the GaN surface, as indicated by RBS/C spectra shown in Fig. 2(b). Table 2 gives implant conditions for which the effect of damage saturation in the crystal bulk has been reported in the literature. Such a saturation of bulk disorder, as

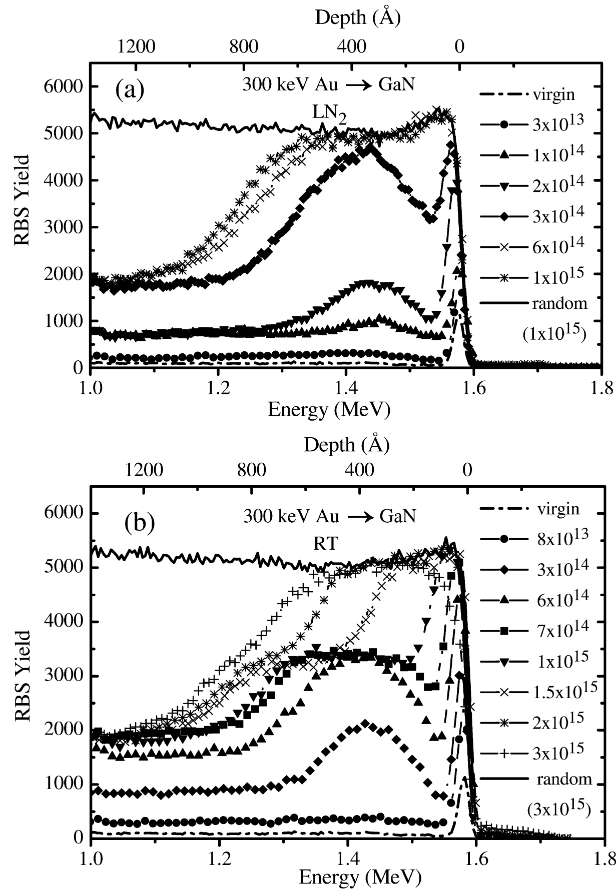

Fig. 2. RBS/C spectra showing the damage build-up for 300 keV Au ion bombardment of GaN at LN_2 with a beam flux of 3.1×10^{12} cm^{-2} s^{-1} (a) and at RT with a beam flux of 4.4×10^{12} cm^{-2} s^{-1} (b). Implantation doses (in cm^{-2}) are indicated in the figure.

illustrated in Fig. 2(b), suggests that the processes of defect production (by the ion beam) and removal (via defect annihilation and, presumably, expansion of the defect band) are balanced during ion irradiation.

2.3. Preferential surface disordering and loss of N

As has been revealed by RBS/C [14,28,30,33], GaN exhibits preferential surface disordering under a wide range of implant conditions (for light and heavy ions, at LN_2 and RT, for different

Table 2
Implant conditions for which the effect of damage saturation in the crystal bulk has been observed

Ion	Energy (keV)	Implantation temperature (°C)	References
^{16}O	600 (60° off normal)	−63	[24]
^{16}O	600 (60° off normal)	−83	[24]
^{197}Au	1000 (60° off normal)	20	[29]
^{197}Au	300	20	[28,33]
^{197}Au	300	550	[37]

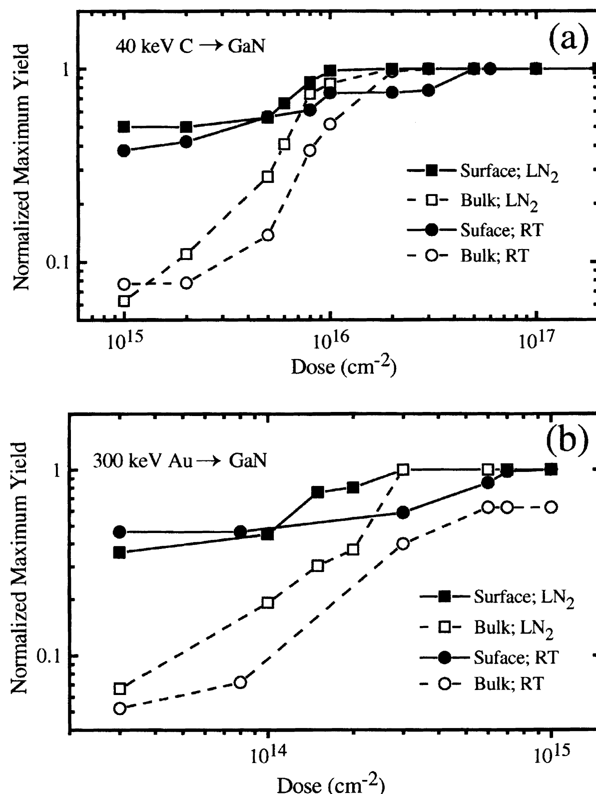

Fig. 3. Dose dependence of the magnitudes of the bulk and surface defect peaks for 40 keV C ion bombardment at LN_2 and RT with a beam flux of 1.4×10^{13} cm^{-2} s^{-1} (a) and for 300 keV Au ion bombardment at LN_2 with a beam flux of 3.1×10^{12} cm^{-2} s^{-1} and at RT with a beam flux of 4.4×10^{12} cm^{-2} s^{-1} (b). The peak levels have been normalized to the random level.

values of beam flux). For example, Figs. 2 and 4 show that the shape of the damage profiles significantly departs from a Gaussian-like defect profile expected based only on the nuclear energy loss processes. Two peaks in the experimental damage distribution are clearly seen (for bombardment with light (Fig. 4) and heavy (Fig. 2) ions at LN_2 and RT), corresponding to surface and bulk peaks of disorder. The bulk peak close to the depth of the maximum nuclear energy loss (for example, ~500 Å in Fig. 2) is not unexpected (see Fig. 1). However, an unusually strong surface peak of disorder in GaN bombarded under a wide range of implant conditions is somewhat surprising. A natural question is "What causes such strong preferential surface disordering?"

The nature of surface disordering has been revealed by XTEM in [30,33,35]. Fig. 5, taken from [33], clearly illustrates the presence of thin surface amorphous layers in GaN implanted with 300 keV Au ions at RT to doses of 8×10^{13} cm^{-2} (Fig. 5(a)) and 7×10^{14} cm^{-2} (Fig. 5(b)). These XTEM images were taken with the electron beam precisely parallel to the GaN surface to eliminate edge effects on the contrast of the near-surface region. As expected, the thickness of the surface amorphous layer in the sample implanted to a dose of 7×10^{14} cm^{-2} is larger than the amorphous layer thickness in the sample implanted to a lower dose of 8×10^{13} cm^{-2}, as seen from Fig. 5(a) and (b). A comparison of RBS/C and XTEM data in [30,33,35] indicated that the strong surface defect peak originated from a thin surface amorphous layer.

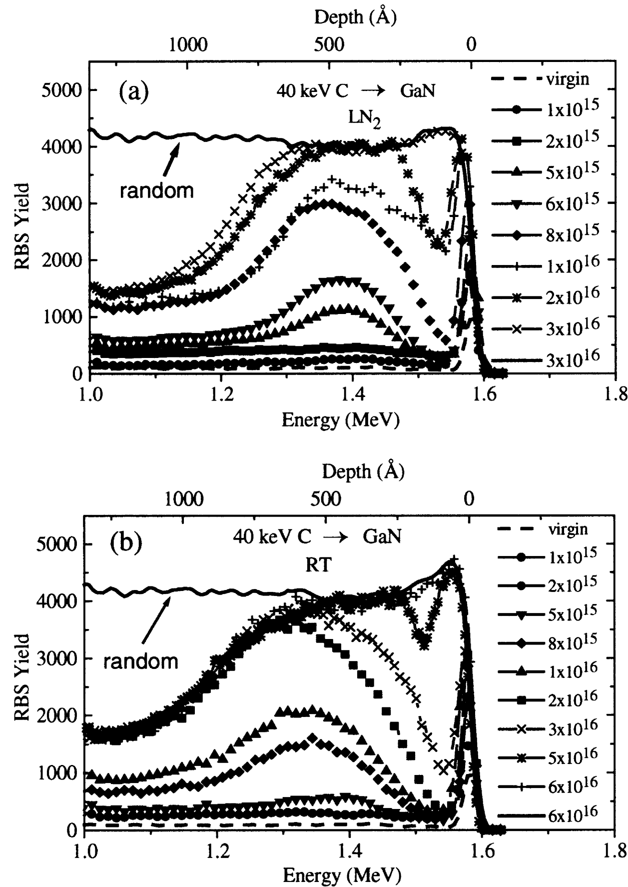

Fig. 4. RBS/C spectra showing the damage build-up for 40 keV C ion bombardment of GaN at LN_2 (a) and RT (b) with a beam flux of 1.4×10^{13} cm^{-2} s^{-1}. Implantation doses (in cm^{-2}) are indicated in the figure.

In contrast to heavy-ion bombardment, XTEM investigation on samples implanted with 40 keV C ions to a relatively low dose[2] of 1×10^{15} cm^{-2} at LN_2 and RT did not reveal any amorphous layer on the GaN surface [33]. In this latter case of low-dose irradiated GaN samples, the strong surface peak in RBS/C spectra has been attributed to the lattice disruption of the first several monatomic layers on the GaN surface due to (i) accumulation of point defects at the GaN surface [33], (ii) ion-produced preferential loss of N [28,30,33], and/or (iii) recoil implantation of the impurities from a thin layer of surface contamination [33]. Such near-surface disorder may act as a precursor for a surface amorphous layer which appears with increasing ion dose. Additional work is desirable to study damage to a GaN surface produced by light-ion bombardment to low doses (see footnote 2).

The RBS/C data from [28,30,33] has indicated that the loss of N from the GaN surface during ion bombardment is not the main reason for preferential disordering in the near-surface region of GaN. It has been suggested that the GaN surface acts as a strong sink for migrating point defects. However, for high-dose implantation, when GaN becomes amorphous, N-deficiency is evident even from RBS/C spectra [28,30,33], although the RBS technique is not very sensitive to the stoichiometry. The random spectra shown in Fig. 2 illustrate an increase in the RBS random yield in

[2] We consider the value of dose to be low or high based on the damage level produced.

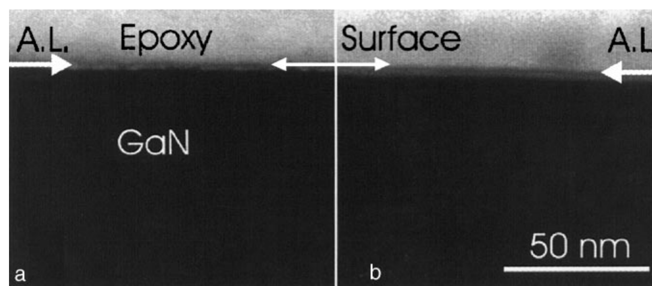

Fig. 5. Cross-sectional bright-field XTEM images of GaN implanted with 300 keV Au ions at RT with a beam flux of 4.4×10^{12} cm^{-2} s^{-1} to doses of 8×10^{13} cm^{-2} (a) and 7×10^{14} cm^{-2} (b). Amorphous layers (labeled as A.L.) on the GaN surface are clearly demonstrated. The thickness of the surface amorphous layer increases with increasing ion dose. The contrast of the XTEM has been adjusted to highlight the amorphous layers, but this causes loss of contrast for bulk depths.

the near-surface region with increasing ion dose. This has been assumed to reflect the loss of N from the surface during ion bombardment [28,30,33]. Moreover, N loss has also been observed by Auger electron spectroscopy after plasma-induced etching of the GaN near-surface region [6,40].

2.4. Defect types

Damage produced in GaN by ion bombardment has been studied by XTEM in [14,16,21,22,27,30,32,33,35–39]. Fig. 6 shows XTEM images ((a), (c), (e) $\boldsymbol{g} = 0\,0\,0\,2^*$ and (b), (d), (f) $\boldsymbol{g} = 1\,\bar{1}\,0\,0^*$) taken from GaN implanted at RT with 300 keV Au ions with a beam flux of

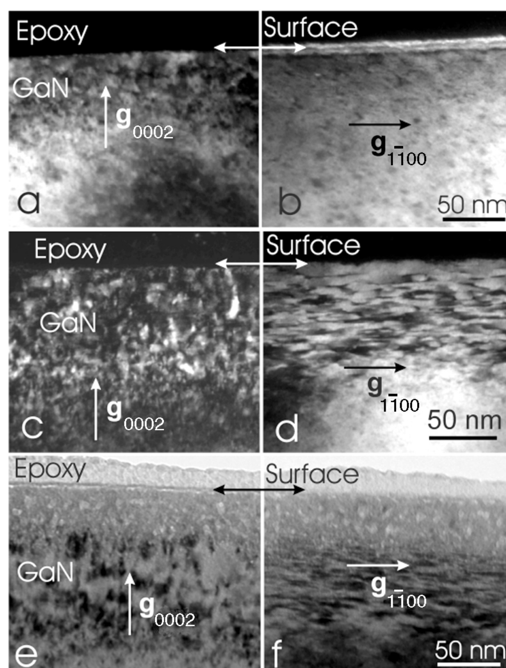

Fig. 6. Dark-field ((a)–(d)) and bright-field ((e) and (f)) XTEM images ((a), (c), (e) $\boldsymbol{g} = 0\,0\,0\,2^*$ and (b), (d), (f) $\boldsymbol{g} = 1\,\bar{1}\,0\,0^*$) of the GaN epilayers bombarded at RT with 300 keV Au ions with a beam flux of 4.4×10^{12} cm^{-2} s^{-1} to doses of 8×10^{13} cm^{-2} ((a) and (b)), 7×10^{14} cm^{-2} ((c) and (d)), and 1.5×10^{15} cm^{-2} ((e) and (f)).

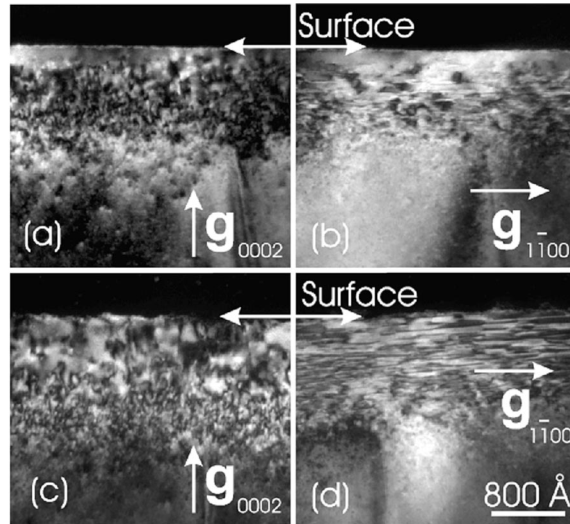

Fig. 7. Dark-field XTEM images ((a), (c) $\boldsymbol{g} = 0002^*$ and (b), (d) $\boldsymbol{g} = 1\bar{1}00^*$) of the GaN epilayers bombarded at 550°C with 300 keV Au ions with a beam flux of 3.1×10^{12} cm^{-2} s^{-1} to doses of 6×10^{14} cm^{-2} ((a) and (b)) and 4×10^{15} cm^{-2} ((c) and (d)).

4.4×10^{12} to doses of 8×10^{13} cm^{-2} (Fig. 6(a) and (b)), 7×10^{14} cm^{-2} (Fig. 6(c) and (d)), and 1.5×10^{15} cm^{-2} (Fig. 6(e) and (f)). Some defect clusters are seen in the implanted region of the sample bombarded to the lowest dose of 8×10^{13} cm^{-2} (Fig. 6(a)). XTEM images from the samples implanted to higher doses (7×10^{14} and 1.5×10^{15} cm^{-2}) clearly illustrate point defect clusters (Fig. 6(c) and (e)) and a band of large planar defects (Fig. 6(d) and (f)) produced by heavy-ion bombardment. These planar defects are parallel to the basal plane of the GaN film. It is also seen from Fig. 6(d) that the region between the surface and the bulk defect peaks is free from planar defects. Fig. 6(e) and (f) illustrate a relatively thick surface amorphous layer (~400 Å thick) in the sample implanted to a dose of 1.5×10^{15} cm^{-2}. Fig. 6(f) also shows that, in the saturation regime for RT bombardment (see Fig. 2(b)), damage in the bulk consists of large planar defects in addition to some defect complexes revealed in Fig. 6(e) taken under different diffraction conditions.

Fig. 7 shows dark-field XTEM images taken from GaN implanted at 550°C with 300 keV Au ions to doses of 6×10^{14} cm^{-2} (Fig. 7(a) and (b)) and 4×10^{15} cm^{-2} (Fig. 7(c) and (d)). The $\boldsymbol{g} = 0\,0\,0\,2^*$ XTEM images shown in Fig. 7(a) and (c) indicate the presence of point defect clusters in the near-surface region (up to ~1500 Å from the GaN surface). In addition, $\boldsymbol{g} = 1\,\bar{1}\,0\,0^*$ XTEM images from Fig. 7(b) and (d) again reveal implantation-produced planar defects. The concentration of these planar defects, which again are parallel to the basal plane of the GaN film, increases with increasing ion dose, as seen from a comparison of Fig. 7(b) and (d).

A similar band of planar defects, as shown in Figs. 6 and 7, has been observed in GaN bombarded with 40 keV C ions and with 100, 300, and 2000 keV Au ions at LN_2 and RT [33,35], with 300 keV Au ions at 550°C [37], and with 2000 keV Cu ions at 500°C [39]. Consequently, it can be concluded that these planar defects represent defect structures characteristic for GaN bombarded with ions under a wide range of implant conditions. However, their microscopic structure and formation mechanisms are not understood at present and warrant additional systematic studies. These planar defects have been assumed to provide a 'nucleation site' for amorphization with further increasing ion dose during bombardment with light or heavy ions at LN_2. However, it appears

energetically favorable for such planar defects to grow rather than to nucleate an amorphous phase for heavy-ion irradiation at RT. Additional studies are highly desirable to understand the evolution and saturation of defects in GaN during ion bombardment.

2.5. Effect of implant conditions

2.5.1. Ion mass

Given the current understanding of ion-beam-induced disordering processes in mature semiconductor materials such as Si and GaAs, one can select two limiting cases based on the characteristics of the collision cascades generated by energetic ions penetrating through a crystal [41]. These two cases are bombardment with light and heavy ions relative to the masses of the host atoms of the material under bombardment. In the case of light ions, collision cascades are very dilute and consist mostly of simple point defects such as vacancies and interstitials. In the case of heavy ions, where the nuclear energy loss rate is large, it is generally believed that each ion generates a dense collision cascade which, upon very fast cascade quenching, can often result in an amorphous zone [8–10]. Bombardment by intermediate mass ions represents a combination of these two limiting cases.

A detailed study of damage build-up in GaN under light (^{12}C) and heavy (^{197}Au) ion bombardment was recently reported in [33]. Indeed, the RBS/C data shown in Figs. 2–4 was taken from [33]. The following similarities between these two irradiation regimes have been pointed out [33].

1. Substantial dynamic annealing of ion-produced defects has been observed for both regimes at LN_2 and RT.
2. For both irradiation regimes, the damage–depth profile, as measured by RBS/C, has two peaks — the surface and bulk defect peaks. This feature has been attributed to high defect mobility and high efficiency of the GaN surface for trapping of migrating point defects [28,30,33].
3. In both cases, a band of planar defects nucleates in the crystal bulk with increasing ion dose.
4. Similar damage build-up behavior at LN_2 has been observed for both light and heavy ion bombardment.

However, the following differences between light and heavy ion bombardment regimes have also been revealed [33].

1. Completely different damage accumulation behavior has been observed for RT bombardment by light (^{12}C) and heavy (^{197}Au) ions (see Figs. 2–4). No damage saturation in the GaN bulk during irradiation with light ions has been observed, as measured by RBS/C. This fact may be explained by the difference in the defects formed during bombardment with light and heavy ions (for example, different size of planar defects). However, the chemical effects of implanted carbon and/or gold atoms may also influence the build-up of radiation damage in GaN, and this requires additional study.
2. A comparison of the disorder levels, as measured by RBS/C, with the results of TRIM calculations [11] has shown that the defect annihilation efficiency is higher for light-ion bombardment than that for irradiation with heavy ions. This result is consistent with the fact that the defect generation rate is larger in the case of heavy-ion bombardment. Such an increase in the generation rate of defects enhances the rate of interaction between mobile defects, and, consequently, promotes the formation of defect complexes rather than defect annihilation via dynamic annealing.

3. Different dependencies of the magnitude of the surface defect peak on beam flux have been observed for light and heavy ions (see Section 2.5.4 for details).

2.5.2. Ion energy

The effect of ion energy on implantation disorder in GaN has been studied in [33,35]. Fig. 8 illustrates that the main features of damage build-up do not change upon increasing the energy of Au ions from 100 to 2000 keV. One can see the same highly sigmodal damage build-up and the nucleation of two amorphous layers (surface and buried) for all three ion energies. In all three cases, the two amorphous layers — at the surface and in the bulk — nucleate and grow via a layer-by-layer amorphization process with increasing ion dose, as has been confirmed by XTEM [33,35]. Ultimately, with further increasing ion dose, these two layers meet, resulting in a thick surface layer of amorphous material.

2.5.3. Implantation temperature

One way to avoid high levels of undesirable ion beam damage is elevated temperature implantation. This fact may explain why the effect of substrate temperature on implantation disorder

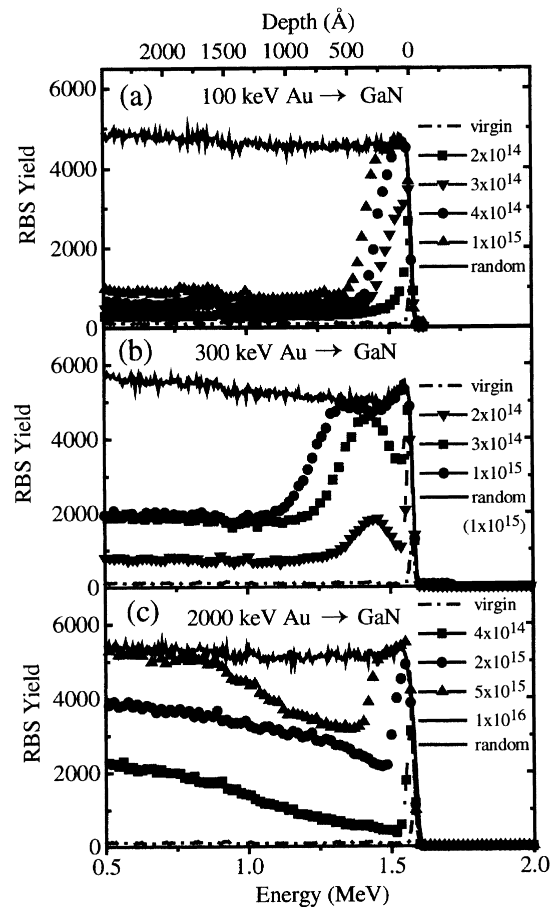

Fig. 8. RBS/C spectra illustrating the damage build-up in GaN bombarded at LN_2 (a) by 100 keV Au ions with a beam flux of 1.4×10^{13} cm^{-2} s^{-1}; (b) by 300 keV Au ions with a beam flux of 3.1×10^{12} cm^{-2} s^{-1}; and by 2000 keV Au ions with a beam flux of 5×10^{12} cm^{-2} s^{-1}. Implantation doses (in cm^{-2}) are indicated in the figure.

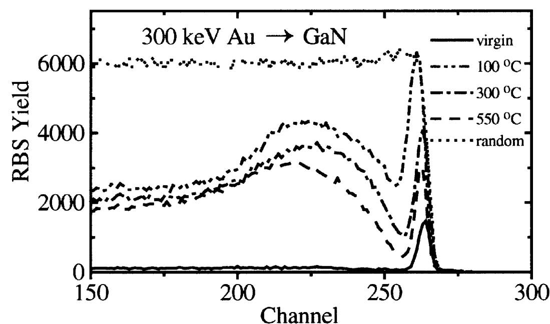

Fig. 9. RBS/C spectra illustrating the effect of implantation temperature on damage produced in GaN by 300 keV Au ion bombardment to a dose of 6×10^{14} cm^{-2} with a beam flux of 4.4×10^{12} cm^{-2} s^{-1}. Implantation temperatures are indicated in the figure.

in GaN has attracted particular interest. For example, Parikh et al. [17] studied, by RBS/C and XTEM, GaN bombarded with 120 keV Mg and 160 keV Si ions at 550°C. Suvkhanov et al. [20] reported a RBS/C study of GaN bombarded at 700°C with 100 keV Si and 80 keV Mg ions. A further report by Wenzel et al. [26] concentrated on lattice disorder produced by a moderate dose of 90 keV Mg ions implanted into GaN at temperatures up to 550°C, as studied by RBS/C. Finally, Kucheyev et al. [37] recently performed a study of damage build-up in GaN under 300 keV Au ion bombardment at 550°C. Results from [17,20,37] have shown that accumulation of stable defects and amorphization are indeed suppressed at elevated temperatures, as compared to implantation at room temperature and below. However, it is very interesting that, for high-dose ion implantation, dramatic ion-beam-induced erosion of the GaN film has been reported [37], which will be discussed in Section 4.

Fig. 9, as well as Figs. 2–4, illustrates the effect of implantation temperature on disorder in GaN bombarded with 40 and 300 keV Au ions. It is seen from Figs. 2–4 that an increase in implantation temperature from LN_2 to RT not only reduces implantation damage but also dramatically changes the damage build-up behavior. Indeed, no the damage saturation in the bulk has been observed in the case of implantation with 300 keV Au ions at LN_2 (see Fig. 2(a)). In addition, Fig. 9 shows that a further increase in implantation temperature up to 550°C appreciably reduces the surface defect peak produced by bombardment with 300 keV Au ions, while the bulk damage, as measured by RBS/C, is much less affected by implantation temperature in this temperature interval. This interesting effect has been attributed to the temperature dependence of defect migration and agglomeration [35].

Fig. 10 shows selected RBS/C spectra that illustrate the damage build-up in GaN with increasing dose of 300 keV Au ions at 550°C. It is seen that, for ion doses up to 6×10^{14} cm^{-2}, the damage level both near the surface and in the bulk (with a maximum at ~500 Å from the surface) gradually increases with increasing ion dose. For higher doses, both near-surface and bulk peaks of disorder exhibit saturation at levels which are considerably below the random level.

The microstructure of defects produced in GaN by 300 keV Au ion bombardment at 550°C was previously shown in Fig. 7. It is interesting that defect types and the damage build-up behavior in the bulk during 300 keV Au ion implantation at 550°C are, in fact, very similar to those observed in GaN bombarded with 300 keV Au ions at RT (see Figs. 2(b) and 6). However, in the case of RT implantation, with increasing ion dose, amorphization proceeds layer-by-layer from the GaN surface, and, for a dose of 2.5×10^{15} cm^{-2} of 300 keV Au ions, the whole implanted region is rendered amorphous. In the case of elevated temperature ion bombardment of GaN, amorphization is not

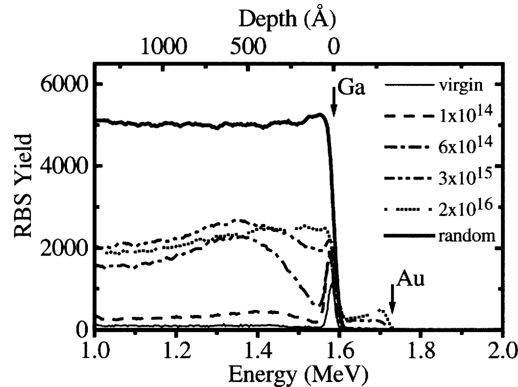

Fig. 10. RBS/C spectra showing the damage build-up for 300 keV Au ion bombardment of GaN at 550°C with a beam flux of 3.1×10^{12} cm^{-2} s^{-1}. Implantation doses (in cm^{-2}) are indicated in the figure. The positions of the surface peaks of Ga and Au are shown by arrows.

observed, but the behavior is more complex due to very efficient ion-beam-induced erosion of the GaN surface for high ion doses [37], as will be discussed in Section 4.

Despite the well-known weakness of the RBS/C technique for determining defect types, the RBS/C study by Wenzel et al. [26] concluded that the defects produced in GaN by 90 keV Mg ions at 25, 300 and 550°C appeared to be the same. This result is in agreement with XTEM data from [33,37,39].

A comment should be made here on the apparent discrepancy in results on elevated temperature ion bombardment of GaN reported in [20,37,39]. Indeed, strong apparent surface disordering observed by RBS/C in [20] in GaN bombarded with 80 keV Mg and 100 keV Si ions at 700°C is not consistent with more recent reports [37,39]. However, more detailed studies by a combination of RBS/C, XTEM, and atomic force microscopy (AFM) techniques [42] have shown that, for elevated temperature bombardment, apparent strong surface disordering, as monitored by RBS/C, can occur but is a result of C contamination of the GaN surface during ion bombardment. Special precautions should be made to suppress such C contamination during high-dose ion bombardment at elevated temperatures.

Another unexpected result has been reported by Wenzel et al. [26]. They have observed that lattice disorder in GaN bombarded with 90 keV Mg ions increases with increasing implantation temperature from RT up to 550°C. A somewhat similar effect of apparently increased damage produced at RT compared to LN_2 temperature for light-ion (40 keV C) bombardment to *low doses* (see footnote 2) was reported in [33]. These interesting results [26,28] may be qualitatively explained based on the fact that an increase in implantation temperature leads to an increase in the rate of all thermally activated point defect processes (defect diffusion, direct and indirect annihilation, formation of complexes, trapping of free defects by defect complexes and impurities, etc.). The nature of 'stable' defect complexes formed at RT or elevated temperatures during dynamic annealing may, as a consequence, result in a higher level of residual disorder. However, at present, further experimental work is necessary to identify the most plausible mechanism for this somewhat odd temperature-dependent effect.

2.5.4. Beam flux

The effect of beam flux on lattice disorder in GaN has been reported in [26,33,35]. Fig. 11 shows RBS/C spectra illustrating the effect of beam flux on implantation damage produced by

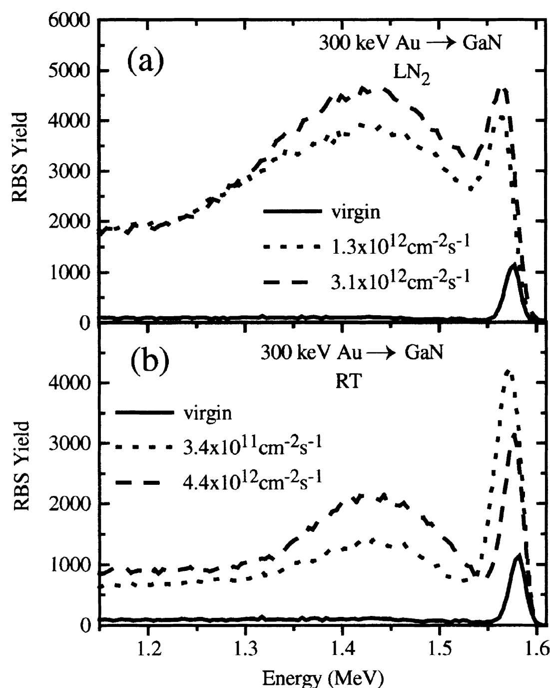

Fig. 11. RBS/C spectra of GaN implanted with 300 keV ions to a dose of 3×10^{14} cm^{-2} at LN_2 (a) and RT (b). The values of beam flux are indicated in the figure. The figure illustrates the reverse and normal flux effects.

300 keV Au ion bombardment of GaN at LN_2 (Fig. 11(a)) and RT (Fig. 11(b)). It is seen that, with increasing beam flux, the magnitude of the bulk defect peak also increases for both LN_2 and RT implantation regimes (the so-called normal flux effect when the damage level increases upon increasing beam flux). This normal flux effect is consistent with the current understanding of ion beam damage build-up in semiconductors under implantation conditions when substantial dynamic annealing of radiation defects takes place (see, for example [4,43]). An increase in beam flux decreases the average time interval between collision cascades which spatially overlap. Such an increase in the generation rate of point defects with increasing beam flux enhances the *rate* of interactions between mobile defects and, therefore, enhances the formation of defect complexes.

However, Fig. 11(b) also shows that, for RT irradiation, the surface defect peak decreases in magnitude with increasing beam flux. This *reverse flux effect*, observed also in the case of light-ion bombardment of GaN at LN_2 [33,35], strongly supports the important role of mobile point defects in the formation and growth of a surface amorphous layer in GaN under ion bombardment. This reverse flux effect has been qualitatively explained in terms of the competition between defect trapping and migration processes [33]. Indeed, an increase in beam flux enhances the formation of defect complexes in the crystal bulk, and fewer point defects can reach the surface. However, Fig. 11(a) shows a normal flux effect for the surface defect peak in GaN under irradiation at LN_2. This has been attributed to smaller effective diffusion lengths of point defects at LN_2, as compared to ion irradiation at RT, where a reverse flux effect has been observed (Fig. 11(b)) [33].

Wenzel et al. [26] have reported that variation of beam flux (from 3.1×10^{12} to 1.3×10^{14} cm^{-2} s^{-1}) of 90 keV Mg ions implanted into GaN at RT has no effect on damage measured by RBS/C. Although this result seems to be somewhat surprising (at least the effects of beam heating could become pronounced for the largest beam flux used), it is consistent with the

independence of implantation disorder on beam flux for light-ion (40 keV C) bombardment of GaN at RT [42].

2.6. Comparison with damage build-up in Si and GaAs

Finally, we make a brief comparison of implantation disorder build-up in GaN with that in much more extensively studied semiconductors — Si and GaAs [33]. All the experimental data on implantation damage in GaN indicates very strong recovery of ion-generated defects in GaN during ion bombardment even at LN_2. In contrast to Si or GaAs, GaN is extremely difficult to amorphize by ion bombardment. For example, amorphous layers in Si or GaAs can be created by heavy-ion bombardment at RT to doses of the order of $10^{14}\,cm^{-2}$, while GaN remains crystalline to much higher ion doses (see for example Figs. 2, 3 and 6). This is a direct consequence of very efficient dynamic annealing processes in GaN during ion bombardment. However, dynamic annealing is never perfect. With increasing ion dose, GaN exhibits layer-by-layer amorphization proceeding from the surface, as well as the nucleation and growth of a band of extended defects in the bulk [33].

Some features of damage build-up in GaN at LN_2 resemble those occurring in Si or GaAs during elevated temperature ion bombardment. Indeed, during elevated temperature ion bombardment of these latter materials, when dynamic annealing of ion-generated defects is strong, damage accumulation proceeds via the formation of an array of extended defects, as has been reviewed elsewhere [4,33,43]. These extended defects in Si or GaAs are usually tangles of dislocations, and their density increases with increasing ion dose. Depending on implant conditions, this can cause a continuous rise in the total energy of the system until it collapses into the energetically more preferable amorphous state [44]. In addition, in both Si and GaAs, layer-by-layer amorphization can proceed from the surface. In this case, the surface acts as a ‘nucleation site’ for amorphization.

Thus, the scenario for amorphization in GaN under ion bombardment even at LN_2 appears to be qualitatively similar to that in Si or GaAs at elevated implant temperatures [33]. Indeed, damage evolution in GaN proceeds via the formation of a band of extended defects under a wide range of implant conditions [33,35,37,39]. The surface of GaN also acts as a ‘nucleation site’ for amorphization [14,15,28–30,33,35,39]. However, the ion-produced extended defects in GaN consist of a regular array of planar defects, not dislocation tangles as in Si or GaAs. Moreover, the presence of a saturation regime during RT bombardment of GaN with heavy ions may suggest that the process of amorphization in GaN is more complex than that in Si or GaAs during elevated temperature bombardment. Indeed, in addition to the possible chemical effects of implanted atoms, amorphization of GaN seems to be stimulated by the processes of local stoichiometric imbalance, which becomes pronounced for high ion doses [33,36,39]. This may explain why amorphous zones, expected from the quenching of dense collision cascades produced by heavy ions, appear to be unstable in GaN, whereas surface and buried amorphous layers can be nucleated for very high ion doses. However, it is obvious that, at present, more experimental work is necessary for a deeper understanding of amorphization mechanisms in GaN.

A comment should be made on the possibility of developing a quantitative model for damage build-up in GaN. It is clear that all ‘traditional’ quantitative models (see, for example [41,45,46]) can be applied only when the rate of dynamic annealing is considerably lower than the defect production rate, which is not the case even for heavy-ion bombardment of GaN at LN_2. At present, the development of a model which takes into account elemental defect processes and dynamic annealing in GaN during ion bombardment appears to be a rather difficult task, due to a very limited understanding of these processes. A satisfactory quantitative model must wait for further experimental insight.

3. Ion-beam-induced porosity

AFM and XTEM results reported in [32,36,39] have shown that high-dose ion bombardment of epitaxial GaN films with heavy ions results in anomalous swelling of the implanted region. For example, an AFM image in Fig. 12 illustrates the border between implanted (on the left) and unimplanted (on the right) areas of a GaN sample bombarded with 2 MeV Au ions at LN_2 to a dose of 1×10^{16} cm^{-2}. As clearly seen, ion implantation has caused pronounced material swelling with a step height as large as ~1700 Å. In addition, the implanted area exhibits large-scale roughness. In Fig. 13 the dose dependence of the step height between implanted and unimplanted regions of 2 MeV Au ion bombarded GaN is shown. It is seen that a rapid step height increase occurs for ion doses above $\sim 3 \times 10^{15}$ cm^{-2}.

In Fig. 14 bright-field XTEM images of GaN bombarded with 2 MeV Au ions at LN_2 to three different doses are shown. Note that all three images were taken with the same magnification. The XTEM image from Fig. 14(a) (a dose of 5×10^{15} cm^{-2}) clearly shows two amorphous layers — surface and buried — separated by a layer of heavily damaged, but still crystalline material. The images from Fig. 14(b) and (c), which are for higher ion doses (doses of 1×10^{16} and 3×10^{16} cm^{-2}, respectively), reveal that ion bombardment to these doses results in the formation of amorphous layers continuous to the surface. Detailed XTEM and electron diffraction investigation performed in [36] showed that these layers were completely amorphous.

Fig. 14 clearly illustrates that GaN amorphized by heavy-ion bombardment is *porous*. The amorphous layers have voids or gas bubbles, which are close-to-spherical in shape. The average radius of the voids/bubbles increases according to the nuclear energy loss profile of Au ions. A comparison of Fig. 14(a)–(c) indicates that, with increasing ion dose, the size of the voids/bubbles also increases. Fig. 14 also suggests that small voids/bubbles agglomerate into larger ones with increasing ion dose.

As reported in [32], the onset of the large step height, with increasing ion dose, coincides with the nucleation of a buried amorphous layer in the region of the maximum nuclear energy loss. Moreover, a rapid step height increase in the dose range from $\sim 3 \times 10^{15}$ to $\sim 7 \times 10^{15}$ cm^{-2} (see Fig. 13) corresponds to the dose interval in which buried and surface amorphous layers expand and

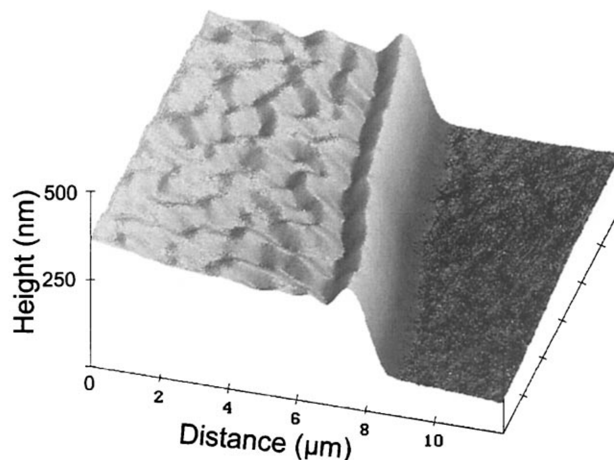

Fig. 12. A tapping mode AFM image illustrating the border between implanted (on the left) and unimplanted (on the right) areas of a GaN sample bombarded with 2 MeV Au ions at LN_2 to a dose of 1×10^{16} cm^{-2} with a beam flux of 5×10^{12} cm^{-2} s^{-1}.

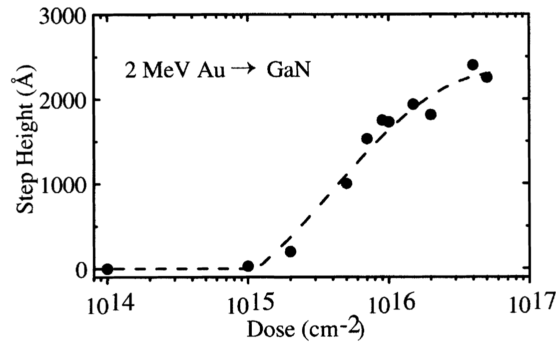

Fig. 13. Dose dependence of the step height between implanted and unimplanted regions of GaN films bombarded with 2 MeV Au ions at LN_2 with a beam flux of 5×10^{12} cm^{-2} s^{-1}.

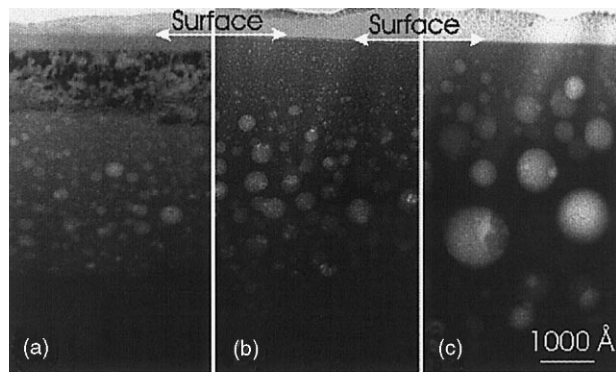

Fig. 14. Bright-field XTEM images of GaN bombarded with 2 MeV Au ions at LN_2 with a beam flux of 5×10^{12} cm^{-2} s^{-1} to doses of 5×10^{15} cm^{-2} (a), 1×10^{16} cm^{-2} (b), and 3×10^{16} cm^{-2} (c). All three images are of the same magnification.

finally overlap, resulting in a thick continuous layer of amorphous material. These results indicate that ion-beam-induced porosity and concomitant material swelling are effects observed in *amorphous* GaN. Relatively small material expansion (see Fig. 13) for ion doses below the threshold for amorphization in the GaN bulk has been partly attributed to the swelling caused by the formation of a thin surface amorphous layer [32], attributed to the trapping of migrating point defects by the GaN surface or amorphous/crystalline interface [30,33,35] (see Section 2).

With increasing ion dose, implantation also causes large-scale surface roughness, which occurs only when buried and surface amorphous layers meet, as shown in Fig. 14. Further ion bombardment to doses above $\sim 3.5 \times 10^{16}$ cm^{-2} results in the formation of craters on the sample surface. Fig. 15 shows AFM images of virgin GaN (Fig. 15(a)) and of GaN bombarded with 2 MeV Au ions at LN_2 to doses of 1×10^{16} (Fig. 15(b)) and 4×10^{16} cm^{-2} (Fig. 15(c)). It is clearly seen from this figure that high-dose heavy-ion bombardment dramatically changes the surface morphology of GaN.

The above evolution of the surface morphology with increasing ion dose has been explained as follows [36,39]. Material swelling in the direction perpendicular to the sample surface is a direct consequence of ion-beam-induced porosity of amorphous GaN, while large-scale surface roughness reflects the relief of stress associated with lateral expansion of the amorphized GaN film. In the case when two amorphous layers are formed (as illustrated in Fig. 14(a)), a stiff layer of crystalline GaN[3]

[3] Even at elevated temperatures, implantation disorder effectively accumulates with increasing ion dose because dynamic annealing processes are never perfect.

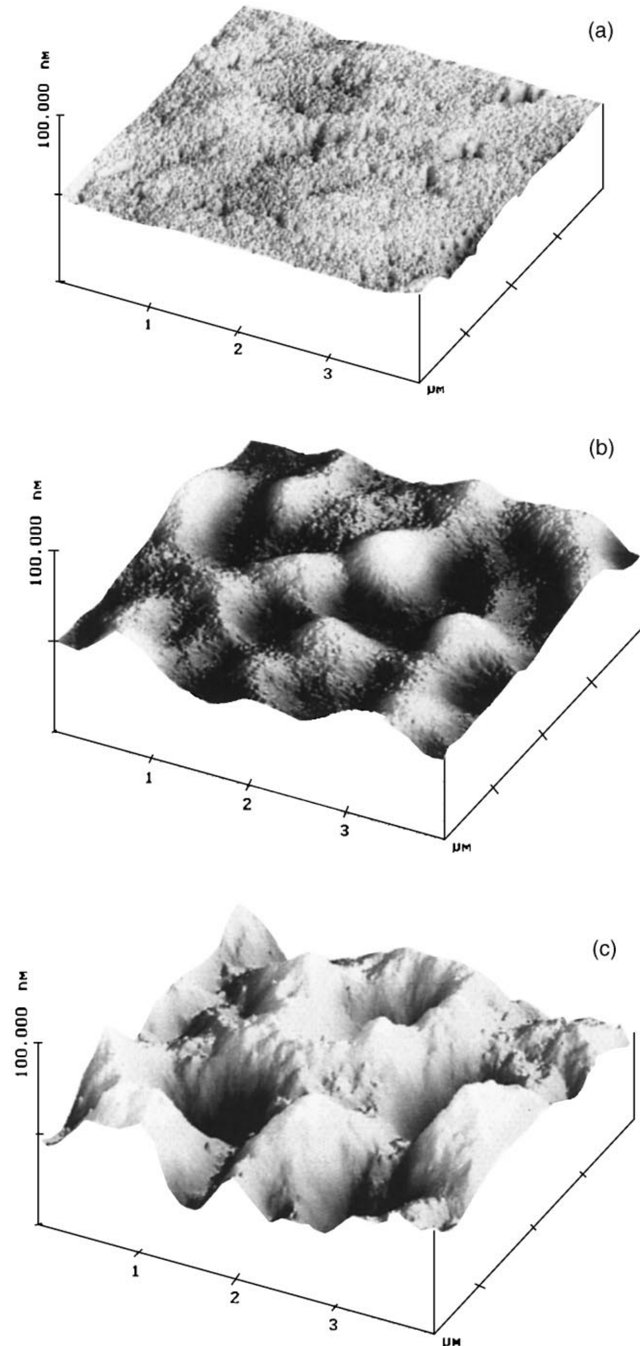

Fig. 15. Height-mode AFM images of virgin GaN (a) and of GaN bombarded with 2 MeV Au ions at LN_2 with a beam flux of 5×10^{12} cm^{-2} s^{-1} to doses of 1×10^{16} cm^{-2} (b) and 4×10^{16} cm^{-2} (c).

separating these two amorphous layers prevents film deformation and, therefore, prevents the appearance of large-scale surface roughness, as consistent with AFM data from [36]. Finally, surface craters observed on samples implanted to high ion doses ($\geq 3.5 \times 10^{16}$ cm^{-2}; see Fig. 15(c)) may be formed when voids/bubbles increase in size and intersect the surface.

It should be noted that similar porous structures have also been observed in GaN films amorphized by 300 keV Au ion bombardment [32,36]. However, in this latter case of keV heavy-ion bombardment, the ion penetration depth is significantly smaller than that in the case of MeV ion irradiation, which makes the material swelling less pronounced. A combination of XTEM, RBS/C, and AFM data has shown that ion-beam-induced volume expansion of amorphous GaN can be as large as $\sim$50% [32,36,39].

The effects of ion-beam-induced porosity and concomitant material expansion reported in [32,36,39] are, in fact, not new. Similar effects have been observed in some other semiconductors, such as Ge [47,48], InSb [49], and GaSb [50]. In general, amorphousness is not necessarily the final state of a semiconductor exposed to ion bombardment. Although, studied in some detail (particularly in the case of Ge [49]), ion-beam-induced evolution of porous structures in amorphous materials is not well-understood. One of the possible explanations for this effect is energetically favorable agglomeration of vacancy-like defects, generated by an ion beam in an amorphous matrix, resulting in the formation of voids [47,48,51]. However, in the case of GaN, ion-beam-induced porosity has been attributed to material decomposition with the formation of N_2 *gas bubbles* in a Ga-rich matrix during heavy-ion bombardment [36,39].

Such a conclusion that the porosity of GaN is due to the formation of N_2 gas bubbles in an amorphous GaN matrix is supported by the evolution of the porous structure with increasing ion dose, as studied by XTEM (see Fig. 14). Indeed, as studied in the cases of ion-beam-induced porosity of Ge, InSb, and GaSb [47–50], the evolution of voids, with increasing ion dose, proceeds via the formation of a sponge-like structure with voids having an elongated, irregular shape. For example, the voids in Ge appear to repel each other as they increase in size [48]. In our case of GaN, the voids/bubbles are spherical in shape for a wide range of ion doses (see Fig. 14), which is typical for the case of the formation of gas bubbles. This conclusion has also been supported by the annealing behavior of porous GaN as well as by RBS/C data [36,39]. Indeed, RBS/C spectra taken from GaN amorphized by heavy ions (see Fig. 2(a)) have a ‘shoulder’ with a decreased RBS/C yield in the ion end-of-range region (a region with large bubbles) and increased yield near the GaN surface (presumably, a Ga-rich region). If a porous layer had voids (not bubbles), no ‘shoulder’ in the RBS/C spectra would be expected [13].

The formation of N_2 gas bubbles has been explained by the well-known effect of ion-beam-induced stoichiometric imbalance [36,39]. Indeed, local stoichiometric imbalance in the collision cascade volume may produce an excess concentration of the heavier element at shallow depth, while the region at greater depth is enriched with atoms of the lighter element. This effect is greatest when the mass ratio of the constituent elements of the semiconductor is high, and when the ion mass is large [52]. Therefore, for the case of 2 MeV ^{197}Au ion bombardment of GaN — a material with a large difference in the masses of constituent elements (^{70}Ga and ^{14}N) — the effect of local stoichiometric imbalance can readily account for the formation of N_2 gas bubbles in a highly N-deficient GaN matrix, as was predicted in [33].

However, the final stoichiometry after ion bombardment also depends on defect migration, not only on the ballistic collisional processes. The data from [32,36,39] suggests that, before amorphization, stoichiometric disturbances in crystalline GaN are very effectively repaired via defect diffusion and dynamic annealing processes. Such dynamic annealing has been shown to be extremely efficient in crystalline GaN (see Section 2). Ion-beam-induced stoichiometric disturbances become evident only after GaN is amorphized (see Fig. 14(a)), as has been shown in [32,36,39].

It should be mentioned that a porous structure similar to that shown in Fig. 14 and discussed above was reported by Liu et al. [22] for GaN implanted at LN_2 with 180 keV Ar ions to a dose of 6×10^{15} cm^{-2}. Fig. 16, taken from [22], shows a XTEM image illustrating a buried layer with large

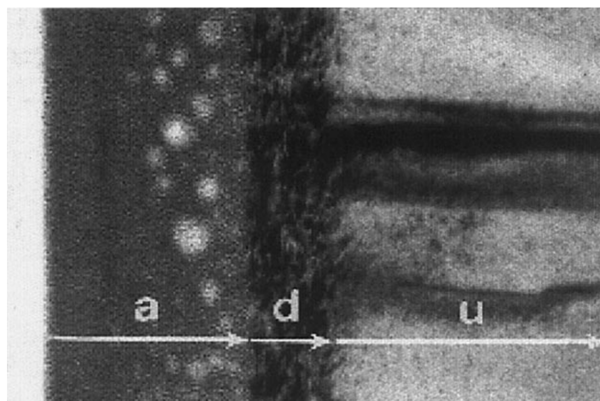

Fig. 16. A bright-field XTEM image of GaN implanted at LN_2 with 180 keV Ar ions to a dose of 6×10^{15} cm^{-2}.

bubbles/voids embedded. Liu et al. [22] claimed that the whole layer (a) in Fig. 16 was amorphous and interpreted the porous-like structure as Ar bubbles. However, in view of the results discussed above, the structure shown in Fig. 16 is more likely to consist of a large concentration of N_2 gas bubbles embedded in an amorphous matrix. Indeed, for a dose of 6×10^{15} cm^{-2} of 180 keV Ar ions, it is very difficult to expect a high concentration of large Ar gas bubbles as shown in Fig. 16. It is more reasonable to interpret Fig. 16 in terms of the phenomenon of ion-beam-induced porosity in GaN. Hence, GaN amorphized with intermediate-mass ions (such as Ar), not only with heavy ions as illustrated earlier in this section, exhibits porosity.

4. Ion-beam-induced erosion

As mentioned above, high-dose ion bombardment of GaN is accompanied by very efficient erosion of the GaN surface. This interesting effect was reported in [37,38,39]. Fig. 17, taken from [37], shows the dose dependence of the step height between implanted and unimplanted regions of GaN bombarded with 300 keV Au ions at 550°C, as measured by AFM. This figure illustrates anomalous surface erosion, which occurs for high ion doses. For example, it is seen that such ion bombardment to a dose of 1×10^{16} cm^{-2} results in the erosion of a ~1000 Å thick surface layer.

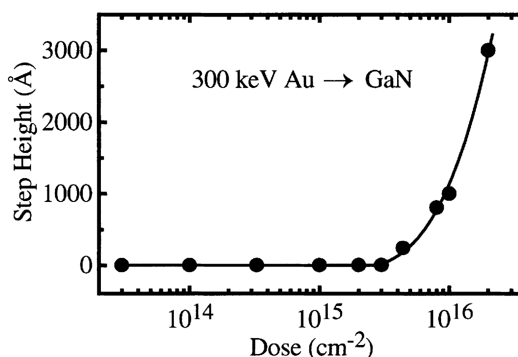

Fig. 17. The dose dependence of the step height between implanted and unimplanted regions of GaN films bombarded with 300 keV Au ions at 550°C with a beam flux of 3.1×10^{12} cm^{-2} s^{-1}. This figure illustrates that high-dose ion implantation is complicated by very efficient material erosion.

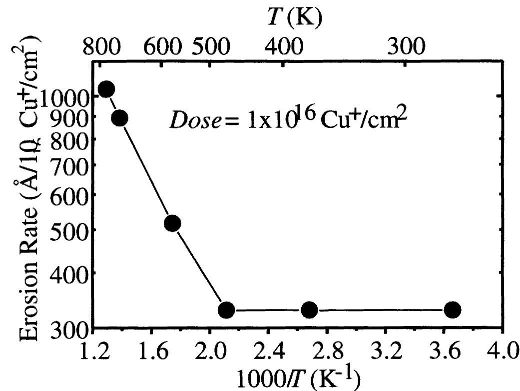

Fig. 18. An Arrhenius plot of the rate of reduction of the amorphous layer thickness for 2 MeV Cu ion bombardment for a dose of 1×10^{16} cm^{-2}.

This anomalous erosion also explains the somewhat unexpected shape of the RBS/C spectra of GaN implanted at 550°C to high ion doses, as illustrated in Fig. 10 for the case of a sample implanted to a dose of 2×10^{16} cm^{-2}. Indeed, due to erosion, the position of the GaN surface changes with increasing ion dose, and both disorder and Au profiles are shifted towards the surface [37].

It is clear that ballistic sputtering mechanisms alone cannot account for such a large sputtering yield for high ion doses (see Fig. 17) [53]. Instead, this anomalous surface erosion has been attributed to a three-step process of (i) the build-up of implantation disorder with increasing ion dose[4] (ii) thermally- and ion-beam-induced decomposition of a heavily damaged near-surface layer for relatively high ion doses, and (iii) ion-beam-induced erosion of such a decomposed (N-deficient) layer [37–39]. This three-step scenario is consistent with recent ion-beam-induced erosion observations for both *amorphous* and *heavily damaged* GaN films. For example, RBS/C data from [38] has shown that the thickness of amorphous layers, produced by low temperature heavy-ion bombardment, reduces almost linearly with increasing dose of 2 MeV Cu ions implanted at 500°C. In addition, Fig. 18 illustrates the temperature dependence of the reduction in the amorphous layer thickness for 2 MeV Cu ion bombardment to a dose of 1×10^{16} cm^{-2}. A XTEM investigation [38] of these samples has shown that such a reduction in the thickness of amorphous layers is due to enhanced ion-beam-induced erosion of the GaN surface, rather than due to ion-beam-induced epitaxial crystallization (IBIEC) [54]. Therefore, data reported in [37–39] indicates that GaN crystals with damage levels above some threshold value exhibit very efficient erosion during elevated temperature ion bombardment. This efficient erosion may impose significant limitations on the technological applications of 'hot implants' into GaN.

5. Mechanical properties

There has been considerable interest in determining the mechanical properties of GaN. Indeed, studies of the processes controlling contact damage, wear, and cracking of GaN layers have significant technological importance. Moreover, understanding the deformation behavior of ion-beam-modified GaN is not only important for contact damage issues in the GaN industry but is also necessary for understanding the evolution of the structural characteristics of GaN under ion bombardment.

[4] The mechanical properties of ion-beam-modified GaN, supporting this discussion, will be discussed in Section 5.

The mechanical properties of semiconductors are usually studied (i) by conventional Vickers micro-hardness testing, or (ii) by continuous-depth-sensing indentation testing (generally known as nanoindentation), which is a much more powerful technique. Indeed, nanoindentation is capable of providing information on a range of mechanical properties such as hardness and elastic properties and their variation continuously with indenter penetration depth. Such information can be readily obtained directly from force–displacement measurements. In addition, nanoindentation is ideal for measuring the mechanical properties of very thin films. It is well-known that, if the substrate is harder than the film, the substrate influence is usually negligible when the penetration depth of the indenter is less than ~10% of the film thickness [55].

Several studies of the mechanical properties of as-grown GaN [56–63] and ion-beam-modified GaN [64] have been reported in the literature. In this section, we discuss the mechanical properties of (i) as-grown GaN, (ii) crystalline GaN with a relatively high concentration of implantation-produced defects, and (iii) GaN amorphized by ion bombardment. It is interesting that, unlike the situation for Si [65], implantation damage dramatically changes the deformation behavior of GaN.

Table 3 gives the values of hardness and Young's modulus of as-grown GaN in comparison with the values for some other semiconductors. It is seen from this table that as-grown GaN is a relatively hard material. In addition, recent nanoindentation data [63] has shown that cracks are not nucleated in GaN epilayers even for loads as large as 900 mN with an ~4.2 μm spherical indenter, which supports a large fracture toughness of this material in the as-grown state.

Fig. 19 shows typical continuous load–unload force–displacement curves of as-grown (Fig. 19(a)), 'ion-damaged' (Fig. 19(b)), and amorphized (Fig. 19(c)) GaN films. Such an 'ion-damaged' sample, with a relatively high concentration of implantation-produced defects (but not amorphous), was prepared by multiple-energy bombardment with ^{197}Au ions at 300°C. The implant conditions used to prepare this sample are given in Table 4. Such a multiple-energy implantation procedure at an elevated temperature results in the formation of lattice defects, including some planar defects, up to ~1 μm from the surface (see Section 2). It should be noted that, for the ion doses used to prepare this sample, the concentration of implanted Au species (<0.06 at.%) is expected to have a negligible effect on the mechanical properties of GaN. Rather, the deformation behavior of ion-beam-modified GaN should be determined by implantation-produced lattice disorder and its consequences.

To prepare an amorphous layer shown in Fig. 19(c), GaN was bombarded with 2 MeV ^{197}Au ions at LN_2 with a beam flux of 5×10^{12} cm^{-2} s^{-1} to a dose of 1.5×10^{16} cm^{-2}. Such implantation results in the formation of an ~0.6 μm thick, completely amorphous surface layer [32,36,65]. It

Table 3
The values of hardness, H, and Young's modulus, E, of as-grown GaN in comparison with the values for some other semiconductors[a]

Semiconductor	H (GPa)	E (GPa)	Plastic penetration (nm)
GaN	13.4	233	100
Si	11.5	150	100
Ge	8.8	118	100
GaAs	7	94	200
InP	4.8	77	200
GaP	9.6	113	300

[a] Data is taken from [63,64,66]. In all the cases, nanoindentation was done with the same spherical indenter, as described in detail elsewhere [64]. The values are chosen for indenter penetration after the 'pop-in' event, as indicated in the last column.

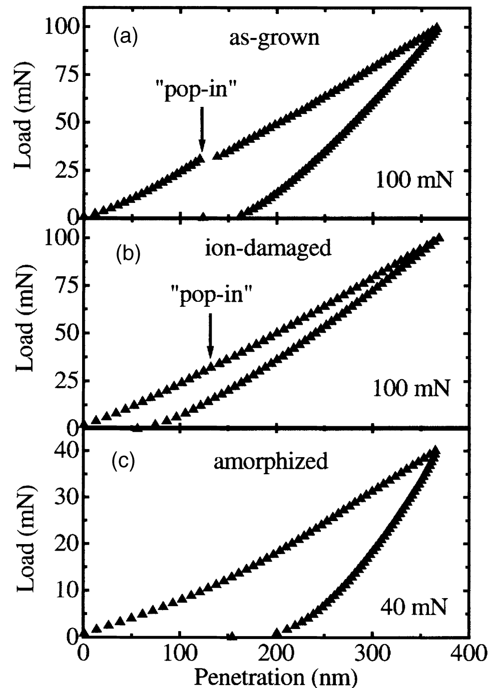

Fig. 19. Typical continuous load–unload curves of (a) as-grown, (b) 'ion-damaged', and (c) amorphized GaN films. Note that the maximum load is 100 mN for (a) and (b) and is 40 mN for (c).

should be noted that GaN amorphized under these conditions should exhibit some degree of porosity (see Section 3), which may also affect the deformation behavior as discussed below.

Fig. 19(a) clearly illustrates that a discontinuity (or 'pop-in') of the yield response occurs during loading of as-grown GaN. This result is in agreement with other nanoindentation data reported in the literature for GaN, as discussed in detail in [63,64]. Interestingly, Fig. 19(b) reveals that in 'ion-damaged' GaN, the 'pop-in' event is still present but significantly less pronounced than in as-grown GaN. Finally, Fig. 19(c) shows no discontinuities in the load–displacement curve of amorphous GaN, in full agreement with the expected deformation behavior of an amorphous solid [65].

Typical amplitude-mode AFM images of as-grown (Fig. 20(a)) and 'ion-damaged' (Fig. 20(b)) GaN films indented at a maximum load of 100 mN are shown in Fig. 20. These AFM images clearly illustrate that slip, which occurs during loading of as-grown GaN, is strongly suppressed in 'ion-damaged' GaN. A comparison of nanoindentation data (see Fig. 19(a) and (b)) and AFM data (see Fig. 20) gives a compelling argument that slip nucleation (rather than a phase transformation) is the physical mechanism responsible for the 'pop-in' events observed during loading of GaN, as discussed more fully in [63,64].

Table 4
The implant conditions used to prepare the 'ion-damaged' sample by multiple-energy bombardment with ^{197}Au ions at 300°C

Energy (MeV)	Dose (10^{14} cm^{-2})	Beam flux (10^{12} cm^{-2} s^{-1})
6.6	7	5.2
2	3	18
0.45	5	17

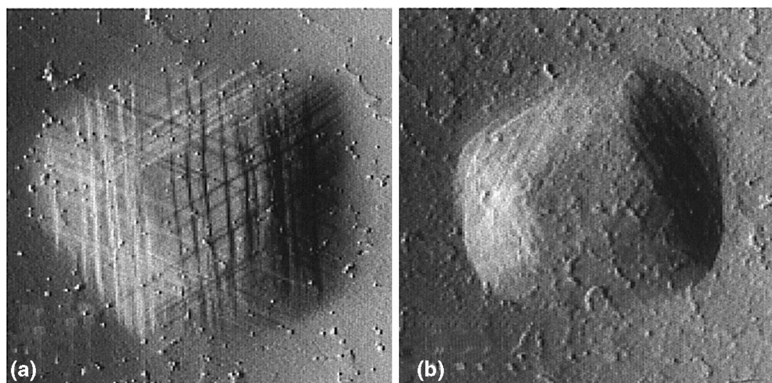

Fig. 20. Typical amplitude-mode AFM images of (a) as-grown and (b) 'ion-damaged' GaN films indented at a maximum load of 100 mN (horizontal field width is 4 μm for both images (a) and (b)).

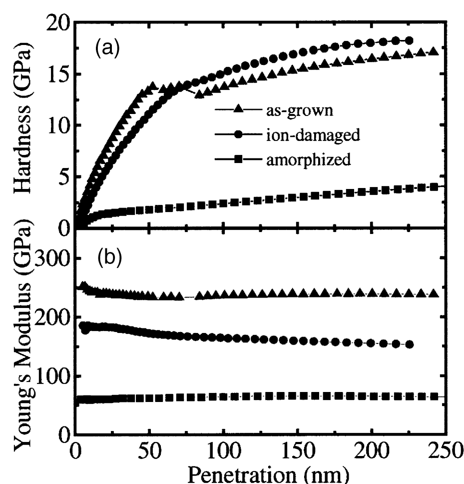

Fig. 21. The curves of (a) the hardness and (b) Young's modulus as a function of indenter penetration below the circle of contact, as determined from the partial load–unload data. Figures show data for as-grown, 'ion-damaged', and amorphized GaN, as indicated in the legend in (a).

Fig. 21 shows the curves of the average contact pressure (or (Meyer) hardness), H (Fig. 21(a)), and Young's modulus, E (Fig. 21(b)), as a function of indenter penetration below the circle of contact, as determined from the partial load–unload data. This figure, showing data for as-grown, 'ion-damaged', and amorphized GaN, reveals that ion bombardment dramatically modifies H and E. It is seen that, for shallow penetration depths of the indenter (prior to the 'pop-in' event), the H and E values of 'ion-damaged' GaN are lower than those of as-grown material. As expected, the value of E is not affected by slip and remains essentially constant for the whole indenter penetration depth[5]. However, slip significantly affects H of as-grown GaN, while in 'ion-damaged' GaN slip is strongly suppressed, and, for larger depths of indenter penetration, H becomes larger than that of as-grown

[5] Slightly non-constant behavior for E of ion-damaged GaN with increasing penetration depth (see Fig. 21(b)) may be attributed to a non-uniform distribution of implantation disorder and/or to the substrate effect.

Table 5
The values of hardness, H, and Young's modulus, E, at a plastic penetration depth of 100 nm for the three GaN samples described in the text

GaN sample	H (GPa)	E (GPa)
As-grown	13.4	233
'Ion-damaged'	15.1	164
Amorphized	2.4	65

GaN. Fig. 21 also shows that the values of H and E of amorphized GaN are significantly lower than those of as-grown and 'ion-damaged' GaN; i.e. amorphous GaN is very soft. Table 5 gives the values of H and E for the above three GaN samples at a plastic penetration depth of 100 nm, a depth where substrate effects are expected to be small.

Finally, a close examination of partial load–unload curves reveals that, in 'ion-damaged' GaN, the purely elastic regime extends to higher loads and penetration depths than in as-grown GaN. This result indicates that implantation disorder in crystalline GaN somewhat suppresses pressure-induced nucleation and/or propagation of extended defects, the processes which are most likely responsible for the plastic deformation of crystalline GaN [61–64]. In contrast, in amorphized GaN, deformation response is elastic–plastic even for very low loads, and, with increasing load, plastic deformation dominates, with pile-up around the impression (as revealed by AFM), typical for indentation of amorphous solids. Such a difference in the deformation modes of as-grown, 'ion-damaged', and amorphized GaN is also reflected by the depths of residual depression (see Figs. 19 and 20) and the depths of maximum plastic penetration (see Fig. 21) of the above three samples.

6. Annealing of implantation damage

In the semiconductor industry, ion implantation used for electrical and optical doping is always followed by an annealing step. Such annealing is necessary (i) to remove implantation-produced lattice disorder and (ii) to electrically/optically activate implanted species by stimulating their migration into energetically favorable lattice sites. Post-implantation annealing is a very important technological step since device performance is highly dependent on the efficiency of such annealing. Below, we briefly discuss the main results reported in the literature on the annealing of ion implanted GaN. As in previous sections of this review, we emphasize recent data, not discussed in the previous reviews. We will also discuss here only the structural characteristics of GaN, while the effects of annealing on the optical and electrical characteristics of ion implanted GaN will be reviewed in the following sections.

6.1. Approaches to annealing of GaN

Annealing of implantation disorder in GaN is expected to be difficult. Indeed, a general rule of thumb, which is well-known from the 1970s, is that temperatures of $\sim$2/3 of the melting point (in K) are required to remove extended defects in semiconductors. Because the melting point of GaN appears to be very high ($\sim$2500°C, based on calculations by Van Vechten [67]), one can expect that annealing temperatures of $\sim$1650°C are necessary to remove implantation-produced disorder in GaN. At such high temperatures, annealing of GaN is complicated by material decomposition; i.e. by loss of nitrogen from the GaN surface [1–3,5]. Such surface decomposition of as-grown GaN

becomes pronounced for prolonged anneals at temperatures of above ~800°C[6]. Suppression of the surface degradation of GaN during annealing is a challenging problem, given the high temperatures required to remove implantation-produced disorder.

Many attempts to anneal implantation damage in GaN have been reported in the literature [15,17,19,21,23,26–28,31,34,36,38,39,68–92] as summarized in Table 6 for the case of the studies of structural characteristics. It is seen from this table that both conventional furnace annealing and rapid thermal annealing (RTA) have been tried, using mostly annealing temperatures up to 1200°C. This maximum annealing temperature of 1200°C reflects the maximum temperatures usually used in Si and GaAs technologies and the fact that commercial RTA equipment is limited to this temperature.

Table 6 also shows that the following methods have been used to protect GaN from decomposition: (i) the proximity geometry, where GaN samples are placed face-to-face, (ii) annealing of GaN within a SiC-coated graphite susceptor which contains powdered AlN or InN to produce a pressure of nitrogen over GaN, (iii) annealing of GaN in an evacuated quartz ampoule containing elementary Al, (iv) annealing under extreme conditions of nitrogen overpressure (up to ~15 kbar), and (v) capping of GaN surface (before annealing) with a protective layer of another material. Examples of annealing behavior given below will support the expectation that annealing temperatures above 1500°C are necessary for a complete removal of implantation disorder in GaN. At such high temperatures, the only methods which have shown some success to suppress decomposition of GaN are (i) an overpressure of nitrogen (up to 15 kbar) and (ii) capping of GaN surface with AlN layers. The other methods tried cannot protect GaN from decomposition at such high temperatures (~1500°C)[7]. Therefore, normal RTA equipment used for annealing at temperatures up to 1200°C is not geared towards the requirements of GaN (i.e. RTA at temperatures at or above ~1500°C or annealing at such temperatures under a large nitrogen overpressure).

6.2. Annealing of pre-amorphous disorder

All the results on the annealing of implantation-produced disorder in GaN indicate that annealing temperatures below ~1200°C are not sufficient to completely remove damage produced even by low-dose implantation (see footnote 2). For example, Fig. 22 illustrates bright-field XTEM images of a GaN sample bombarded with 90 keV Si ions at LN_2 to a dose of 6×10^{15} cm^{-2}. Shown in Fig. 22(a) and (b) are images before and after post-implantation annealing at 1100°C for 30 s, respectively. Fig. 22(a) shows that such Si ion implantation produced a dense network of defect clusters in the implanted layer, while Fig. 22(b) indicates that annealing at 1100°C does not remove these defects. This has also been confirmed by RBS/C [15]. For example, the annealing of GaN implanted with 90 keV Mg and 180 keV Ca ions was studied by RBS/C in [26,27,31]. It has been shown that significant (but always only partial) recovery of implantation damage by annealing at 1100°C for 15 s in a nitrogen ambient is possible only after very low dose ion implantation (see footnote 2). Such low doses are found to produce very dilute disorder observed by XTEM and RBS/C [33]. Thus, annealing at relatively low temperatures (below ~1200°C) is only effective in significantly reducing implantation damage produced by low-dose ion implantation, before the nucleation of planar defects. For larger ion doses, when a band of extended defects nucleates in the

[6] However, the temperature where decomposition of GaN becomes pronounced strongly depends on the defect state of the material as well as on the annealing ambient.

[7] It should be noted that success achieved with preventing decomposition of GaN by capping the GaN surface with AlN layers is still limited because of a problem with ex-foliation of AlN layers during such an ultra-high temperature RTA treatment.

Table 6
Studies of thermal annealing of GaN (structural characteristics)

Ion	Energy (keV)	Implantation temperature (°C)	Ion dose (10^{14} cm^{-2})	Annealing mode T (°C)	Surface protection	Ambient	Analysis	References
Si	90	−196	0.5–400	RTA ≤ 1100	Proximity	N_2	RBS/C, XTEM	[15,21,85]
Te	350	−196, 20, 200	10	RTA, 1100	Proximity	N_2	RBS/C	[21]
Zn	200	20	0.08–0.2	RTA ≤ 1100	SiN_x cap	N_2	XRD	[16]
Si	160	550	10	RTA, 1000	Proximity	Ar	RBS/C	[17]
Ca	180	−196	0.05–60	RTA ≤ 1150	Proximity	N_2	RBS, XTEM	[27,31]
Mg	90	25, 300, 550	1–50	RTA, 1150	Proximity	N_2	RBS/C	[26,27]
Mg	150	20	0.5	RTA, 1000	Proximity	N_2	XRD	[23]
Be	200	20	5	RTA,1000	Proximity	N_2	XRD	[23]
O	600[a]	−83, −63	0.5–500	Oven ≤ 700	–	Vacuum	RBS/C	[24]
Au	1000[a]	−93, 20	0.4–50	Oven ≤ 600	–	Vacuum	RBS/C	[29]
Au	2000	−196	>100	RTA ≤ 1050	Proximity	N_2	RBS/C, XTEM, AFM	[36,38,39,90]
Er	160	20	5, 50	Oven ≤ 900	Proximity	N_2	RBS/C	[72]
Si	210	20	50	RTA ≤ 1400	AlN cap	N_2	RBS/C	[92]
Si	100	20	50	Oven, 1500	~15 kbar of N_2	N_2	RBS/C	[1]
Si	150	20	5, 50	RTA ≤ 1400	AlN cap	N_2	TEM	[93]

[a] Implantation 60° off surface normal.

crystal bulk [33], much higher annealing temperatures are required for even partial removal of defects.

RBS/C results discussed in [91] have shown that RTA annealing at 1400°C for 30 s of GaN (capped with AlN) implanted with 210 keV Si ions to a dose of 5×10^{15} cm^{-2} at RT resulted in only a partial recovery of implantation-produced lattice disorder. The only report on a successful (and an apparently complete) recovery of implantation damage (produced by 100 keV Si ion implantation to a dose of 5×10^{15} cm^{-2} at RT) involved post-implantation annealing at 1500°C for 15 min under a nitrogen overpressure of ~15 kbar [1]. After such an annealing, the sample had an RBS/C yield equivalent to an unimplanted sample, with no macroscopic surface decomposition [1]. The annealing of damage was also supported by photoluminescence and Hall effect measurements. For the first time, this result has demonstrated that implantation disorder can be effectively removed by ultra-high

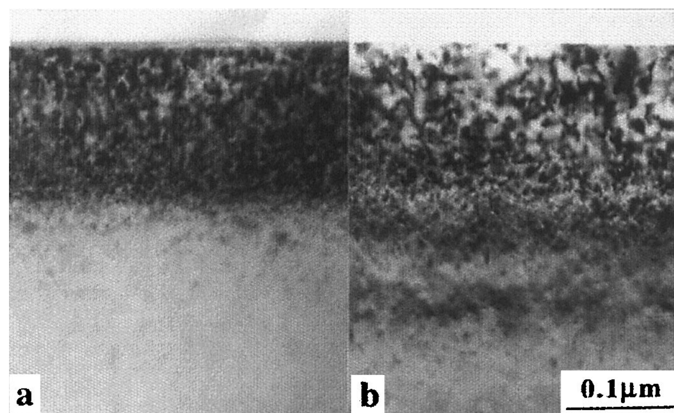

Fig. 22. Bright-field XTEM images of a GaN sample bombarded with 90 keV Si ions at LN_2 to a dose of 6×10^{15} cm^{-2}. Shown are images before (a) and after (b) post-implantation annealing at 1100°C for 30 s.

temperature (1500°C) prolonged (15 min) annealing [1]. However, further work is obviously needed to find alternative ways, besides extremely high pressures of nitrogen, to prevent surface decomposition of GaN during ultra-high temperature post-implantation annealing. Further work is also needed to study the evolution of implantation-produced defects during annealing.

6.3. Redistribution of dopants during annealing

Several studies of the thermal stability of dopants implanted into GaN have been reported in the literature [16,29,69,92–97]. In this section, we concentrate on the most recent dopant redistribution data following 1450°C annealing [92]. For this annealing, it was necessary to cap samples with reactively sputtered AlN films to avoid dissociation.

Secondary ion mass spectrometry (SIMS) profiles of Mg implanted into GaN, both before and after annealing at 1450°C have shown that within the resolution of SIMS (~200 Å under these conditions) there is no motion of Mg. Using a simple $2\sqrt{Dt}$ estimation of the diffusivity at this temperature gives a value of $\leq 2 \times 10^{-13}$ cm^2 s^{-1}. This is in sharp contrast to the behavior of Mg in GaAs [98–100], where the rapid diffusion of the Ga-site acceptors during annealing can only be suppressed by co-implantation of a group V element to create a sufficient number of vacant sites for the initially interstitial acceptor ions to occupy upon annealing. This reduces the effective diffusivity of the acceptor and increases its electrical activation. The additional advantage gained from using a group V co-implant is that it maximizes the occupation of the group III site by the acceptor. In addition, Mg implanted into GaAs often displays outdiffusion toward the surface (in most cases up, rather than down, the concentration gradient), leading to loss of dopant into the annealing cap [101]. This has been suggested to be due to non-equilibrium levels of Ga interstitials created by the implantation process. This mechanism is clearly absent for Mg implanted into GaN.

Fig. 23 shows a series of profiles for ^{9}Be before and after annealing up to 1200°C. Note that there is an initial broadening of the profile at 900°C, corresponding to an effective diffusivity of $\sim 5 \times 10^{-13}$ cm^2 s^{-1} at this temperature. However, there is no subsequent redistribution at temperatures up to 1200°C. Implanted Be shows several types of anomalous diffusion in GaAs, including up-hill diffusion and movement in the tail of the profile, in addition to normal concentration-dependent diffusion [100], which also results from the non-equilibrium concentrations of point defects created by the nuclear stopping process of the implanted ions. It appears that in GaN, interstitial Be undergoes a type of transient-enhanced diffusion until these excess point defects are removed by annealing, at which stage the Be is basically immobile.

Carbon is typically a very slow diffuser in all III–V compounds, since it strongly prefers substitutional lattice sites [1,98–102]. In GaN, it has been shown that it is possible to get p-type conductivity in carbon-doped material, albeit with low hole concentrations. In general, however, GaN containing high concentrations of carbon is self-compensated [1], suggesting that carbon is occupying both Ga and N sites. It is an extremely slow diffuser when implanted into GaN, with $D_{\mathrm{eff}} \leq 2 \times 10^{-13}$ cm s^{-1} at 1400°C [92].

Similar data for Ca implants in GaN showed that once again there was no detectable motion of the acceptor dopant.

Little work has been performed on the diffusion of group VI donors in GaN, although Feng et al. [103] showed that Se displayed relatively high diffusion during growth by metalorganic chemical vaper deposition (MOCVD) at 1000°C. Wilson et al. reported some redistribution of implanted S after annealing at 700–1000°C in relatively thin layers of GaN [93], which might have been influenced by a high defect density in this material. However, more recent SIMS profiles before and after 1450°C annealing of S in GaN have shown that there is clearly no motion of the sulfur under

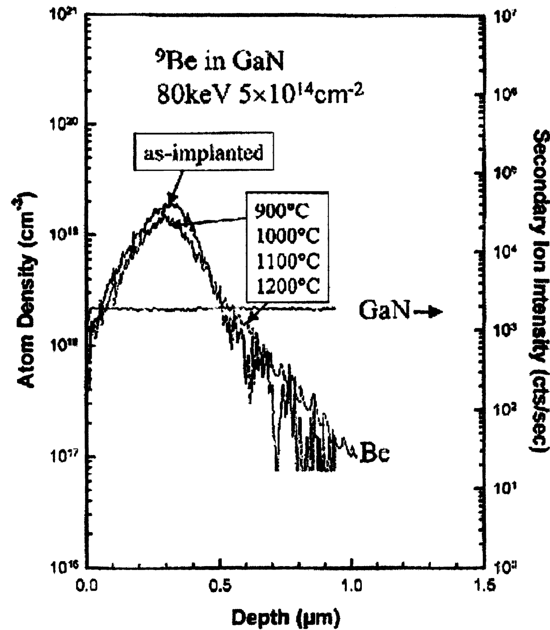

Fig. 23. SIMS profiles before and after annealing at different temperatures of implanted Be (80 keV, 5×10^{14} cm^{-2}) in GaN.

these conditions [92], which suggests that, as expected, the structural quality of the GaN may have a strong influence on the apparent diffusivity of dopants. The samples in this latter case [92] were much thicker than those employed in the previous work [93], and the extended defect density was correspondingly lower in the implanted region ($\sim 5 \times 10^8$ cm^{-2} compared to $\sim 10^{10}$ cm^{-2} in the thin samples).

The other group VI donors, Se and Te, have low diffusion coefficients in all compound semiconductors (for example, $D_{\mathrm{Se}} = 5 \times 10^{-15}$ cm^2 s^{-1} at 850°C in GaAs), and we find a similar result for these species implanted into GaN [92]. Fig. 24 shows the SIMS profiles before and after 1450°C annealing for Se, while Fig. 25 shows similar data for Te. In both cases, the effective diffusivity at this temperature is $\leq 2 \times 10^{-13}$ cm^2 s^{-1}.

SIMS profiles of implanted O before and after 1125°C annealing showed that there was also no detectable redistribution of the oxygen [94].

The redistribution of implanted Si, Mg, and C in $Al_{0.123}Ga_{0.88}N$ was studied by Polyakov and co-workers [104]. While Si and C demonstrated no measurable diffusion by SIMS after a 1140°C, 1 h anneal, Mg did show appreciable profile broadening and indiffusion under these conditions. More work is needed on the effect of Al composition on the implantation properties of AlGaN.

Finally, results on dopant redistribution [92] show the effectiveness of the AlN cap in protecting the GaN surface from dissociation since if any of the surface degraded during annealing, the implant profiles would no longer overlap. Indeed, material decomposition during post-implantation annealing may complicate the interpretation of data on dopant redistribution. This is especially important for heavily damaged GaN, where decomposition starts at much lower temperatures (see Section 6.5). Such decomposition may explain somewhat unexpected RBS/C results reported in [29] on redistribution of Au atoms during post-implantation annealing of GaN amorphized by Au ion bombardment.

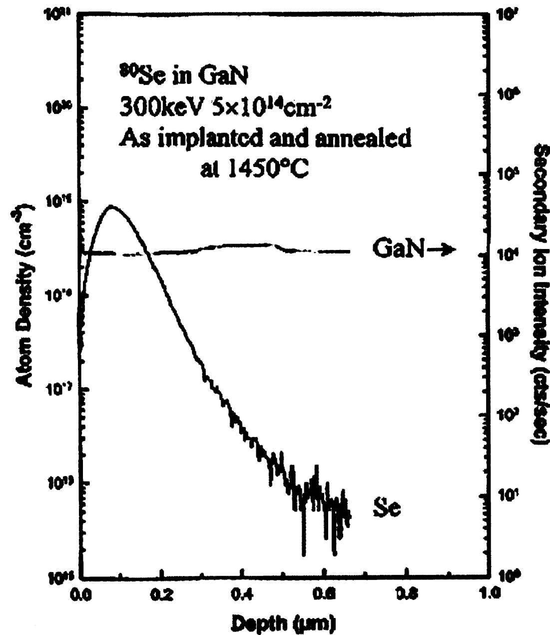

Fig. 24. SIMS profiles before and after annealing at 1450°C of implanted Se (300 keV, 5×10^{14} cm^{-2}) in GaN. The profiles are essentially coincident.

In summary, negligible redistribution has been observed by SIMS for most potential dopants (Be, C, Mg, Si, and Ca) during post-implantation annealing at even 1450°C [92]. This bodes well for the fabrication of GaN-based power devices such as thyristors and insulated gate bipolar transistors, which will require creation of a doped well in source/drain regions by ion implantation. The low

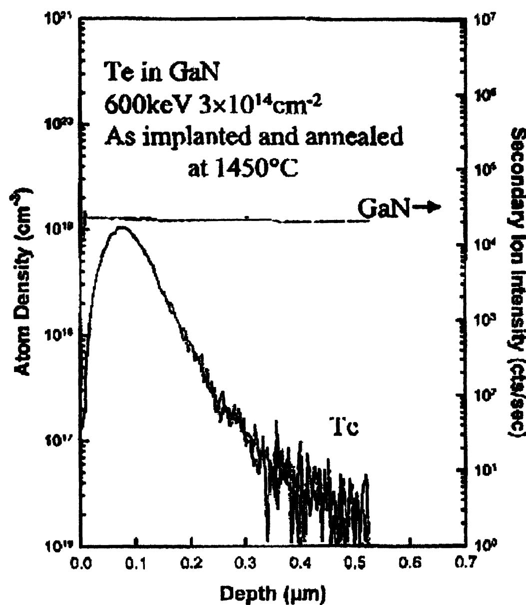

Fig. 25. SIMS profiles before and after annealing at 1450°C of implanted Te (600 keV, 5×10^{14} cm^{-2}) in GaN. The profiles are essentially coincident.

diffusivities of implanted dopants in GaN means that junction placement should be quite precise, and there will be fewer problems with lateral diffusion of the source/drain regions toward the gate.

6.4. Lattice sites of dopants

The electronic structure of dopants in GaN depends on their position in the lattice. Despite the clear importance of dopant lattice sites for electrical and optical applications, only a few such studies have been reported in the literature [21,71–75,78,105], as was reviewed elsewhere [1,5]. Here, we briefly summarize the main results on the lattice sites of dopants in GaN.

It has been shown that a relatively high fraction of implanted Si, Ca, Te, and Er atoms is substitutional even just after implantation [21,71,73,74]. This result is consistent with very efficient dynamic annealing processes in GaN. Indeed, migration and annihilation of ion-beam-generated defects during ion bombardment are expected to promote the migration of implanted species into energetically favorable lattice sites (i.e. substitutional sites in the case of above species). Data from [73,74] suggests that after annealing at 1100°C, most of implanted Si or Ca atoms occupy Ga sites.

Several reports have also been published on the lattice location of rare-earth elements implanted into GaN [71,75,105]. It has been shown that both Er and Pr are thermally stable on substitutional Ga sites.

6.5. Recrystallization of amorphous layers

Only a few reports have been published on the annealing behavior of amorphous layers in GaN [15,21,29,36,38,88,89]. Results from [21,38,88] have shown that thermal annealing of amorphous GaN at temperatures above ~500°C results in polycrystallization, rather than in solid phase epitaxial growth (SPEG). For example, shown in Fig. 26 is an XTEM image showing polycrystallites formed in two amorphous layers (surface and buried amorphous layers) in GaN annealed at 500°C for ~2 h in vacuum. These amorphous layers were prepared by implantation with 0.9 and 0.45 MeV Au ions.

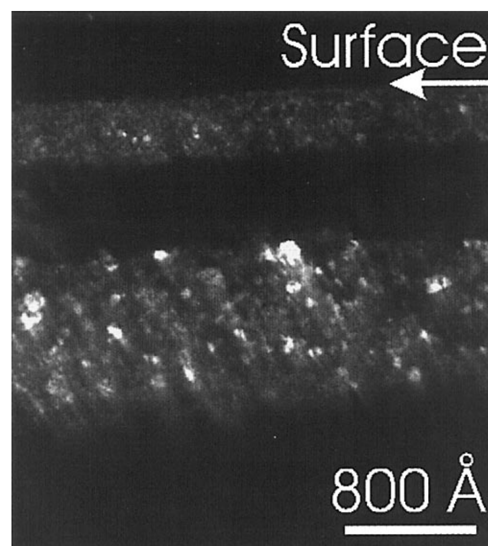

Fig. 26. A dark-field XTEM image showing polycrystallites formed in two amorphous layers (surface and buried amorphous layers) in GaN annealed at 500°C for ~2 h in vacuum. These amorphous layers were prepared by implantation with 0.9 and 0.45 MeV Au ions.

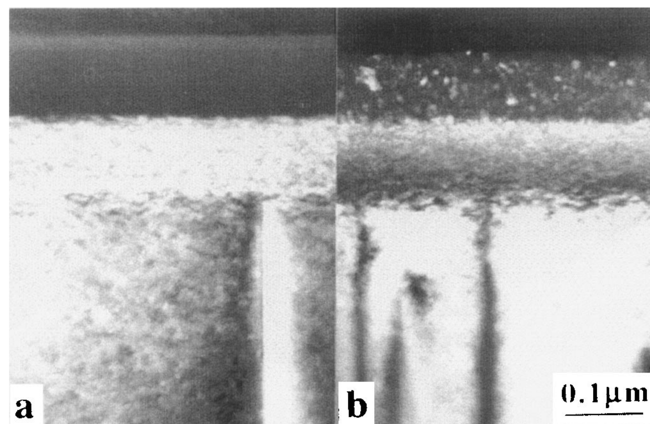

Fig. 27. Dark-field XTEM images of a GaN sample implanted at LN_2 with 90 keV Si ions to a dose of 4×10^{16} cm^{-2}. Shown are images before (a) and after (b) post-implantation annealing at 1100°C for 30 s.

Annealing of amorphous layers produced in GaN by ion bombardment is also complicated by the porosity of amorphous GaN (see Section 3). Due to porosity, GaN amorphized by ion bombardment decomposes during post-implantation annealing at relatively low temperatures (above ~400°C). Decomposition of amorphous GaN has been discussed in [28,30,36,38]. Such decomposition may explain the RBS/C data reported in [15,29,71], which showed a reduction in the amorphous layer thickness on annealing, behavior which was originally interpreted as SPEG. For example, the disappearance of a thin amorphous layer after annealing, as shown in Fig. 22, was attributed to its crystallization [15]. However, a careful examination of the surface roughness of the samples shown in Fig. 22 strongly suggests that removal of the amorphous layer is most likely due to material decomposition, rather than due to SPEG. Such decomposition is also supported by Fig. 27, which shows dark-field XTEM images of a GaN sample implanted at LN_2 with 90 keV Si ions to a dose of 4×10^{16} cm^{-2}. The images before (Fig. 27(a)) and after (Fig. 27(b)) post-implantation annealing at 1100°C for 30 s show that a sample with a relatively thick continuous surface amorphous layer produced by Si ion implantation has a very rough surface after annealing. Furthermore, this layer is thinner than it was before annealing, again presumably due to material decomposition.

Decomposition of amorphous GaN during post-implantation annealing becomes very pronounced for the case of relatively thick surface layers amorphized by MeV heavy-ion bombardment. For example, Fig. 28 shows a typical top view AFM image of GaN amorphized with 2 MeV Au ions (a dose of 1.2×10^{16} cm^{-2}) at LN_2 and subsequently annealed for 10 min at 450°C in a nitrogen atmosphere. This AFM image illustrates the formation of large craters on the surface as a result of decomposition of porous GaN. These craters are ~2–2.5 µm in diameter and ~0.2 µm deep. As expected, the depth of the craters is within the thickness of the GaN layer amorphized by ion implantation. This thermally-induced decomposition of GaN occurs at annealing temperatures above about 400°C [28]. The formation of such craters has been attributed to thermally-induced agglomeration of implantation-produced N_2 gas bubbles into larger bubbles with subsequent surface ex-foliation [36,89].

The results discussed above show that the annealing of amorphous layers in GaN has been decidedly unsuccessful. This result suggests that amorphization of GaN during ion bombardment should be avoided at all costs.

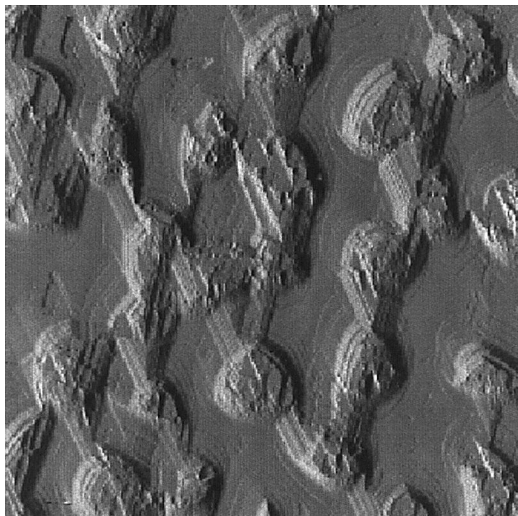

Fig. 28. A typical top-view amplitude-mode AFM image of GaN bombarded with 2 MeV Au ions at LN_2 to a dose of 1.2×10^{16} cm^{-2} with a beam flux of 5×10^{12} cm^{-2} s^{-1} and subsequently annealed for 10 min at 450°C in N_2 atmosphere (horizontal field width is 15 μm).

6.6. Ion-beam-induced reconstruction of amorphous GaN

It is interesting that dramatic decomposition of amorphous GaN during post-implantation annealing can be effectively suppressed by re-irradiation with light ions [89]. Fig. 29 shows a typical AFM image illustrating thermally-induced decomposition of amorphous GaN but also showing the dramatic effect of re-irradiation with light ions. After amorphization with heavy ions, one part of this sample (the left half of the image) was re-irradiated with light ions, while the other part of the sample (the right half of the image) was masked (see the figure caption for the details of implant conditions). Subsequently, this sample was annealed at 450°C for 10 min in a nitrogen atmosphere. Fig. 29 clearly illustrates that light-ion re-irradiation of amorphous GaN effectively suppresses a complete

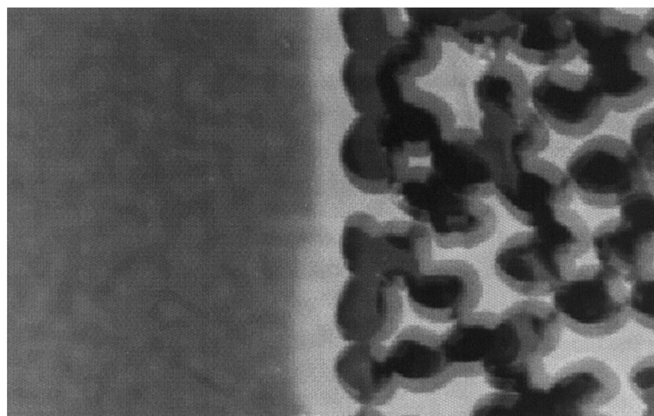

Fig. 29. A top-view height-mode AFM image of a GaN sample amorphized with 2 MeV Au ions implanted at LN_2 (dose = 1.2×10^{16} cm^{-2}, beam flux = 3×10^{12} cm^{-2} s^{-1}). After amorphization, one part of this sample (the left half of the image) was re-irradiated with 1 MeV C ions at RT (dose = 5×10^{15} cm^{-2}, beam flux = 2.5×10^{12} cm^{-2} s^{-1}), while the other part of the sample (the right half of the image) was masked. Subsequently, this sample was annealed at 450°C for 10 min in a nitrogen atmosphere. The horizontal field width of the image is 27 μm.

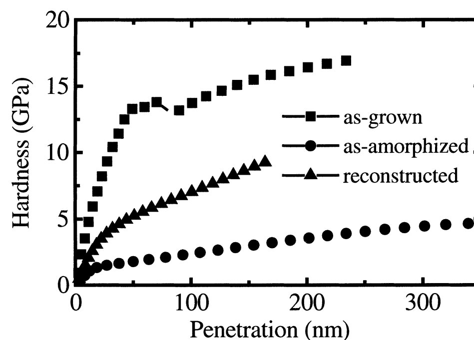

Fig. 30. The curves of hardness as a function of indenter penetration below the circle of contact, as determined from the partial load–unload data. The figure shows data for (i) as-grown GaN, (ii) GaN amorphized with 2 MeV Au ions at LN_2 (dose $= 1.5 \times 10^{16}$ cm^{-2}, beam flux $= 5 \times 10^{12}$ cm^{-2} s^{-1}), and (iii) the same amorphous GaN sample re-irradiated with 1 MeV C ions at RT (dose $= 1 \times 10^{16}$ cm^{-2}, beam flux $= 3 \times 10^{12}$ cm^{-2} s^{-1}), as indicated in the legend. The maximum load was 100 mN for as-grown GaN and was 40 mN for as-amorphized GaN and amorphous GaN re-irradiated with light ions.

decomposition of the material during post-implantation annealing. Moreover, results from [89] show that the formation of craters on the surface of amorphous GaN re-irradiated with light ions does not take place during RTA treatment at temperatures up to 1050°C, the maximum annealing temperature used in [89].

Another effect of light-ion re-irradiation is illustrated by Fig. 30, which shows the curves of the average contact pressure (or (Meyer) hardness) as a function of indenter penetration below the circle of contact, as determined from the partial load–unload indentation data. This figure shows typical curves for (i) as-grown GaN, (ii) as-amorphized GaN, and (iii) amorphous GaN re-irradiated with light ions at RT (see implant details in the figure caption). It is seen from Fig. 30 that the value of hardness of as-amorphized GaN is much lower than that of as-grown GaN. More interestingly, Fig. 30 illustrates that light-ion re-irradiation significantly increases the hardness of amorphous GaN. Table 7 gives the values of hardness and Young's modulus for as-grown, as-amorphized, and light-ion re-irradiated GaN (for the three GaN samples from Fig. 30) at a plastic penetration depth of 100 nm. Such an increase in the values of hardness and Young's modulus as a result of light-ion re-irradiation correlates with the suppression of material decomposition during post-implantation annealing.

Results from [89] show that the changes in the mechanical properties and the suppression of thermally-induced decomposition of amorphous GaN are controlled by the electronic energy loss of light ions. The excitation of the electronic subsystem of amorphous GaN is sufficient to induce a rearrangement of atomic bonds broken during amorphization with heavy ions. These effects of light-ion re-irradiation of amorphous GaN have been attributed to an ion-beam-induced atomic-level reconstruction of the amorphous phase, i.e. to the rearrangement and re-bonding of atomic bonds broken during heavy-ion bombardment used to amorphize GaN. Therefore, high-dose bombardment

Table 7
The values of hardness, H, and Young's modulus, E, at a plastic penetration depth of 100 nm for the three GaN samples from Fig. 30

GaN sample	H (GPa)	E (GPa)
As-grown	14.0	233
As-amorphized	2.4	65
Light-ion re-irradiated	7.0	99

of GaN with heavy ions (like ^{197}Au), which generate very dense collision cascades, produces a metastable amorphous phase of GaN. This amorphous phase can be further reconstructed by bombardment with lighter ions, when ion-generated collision cascades are dilute.

7. Optical properties

The optical properties of GaN have received extensive attention due to their importance in the fabrication of GaN-based optoelectronic devices. One way to modify the optical characteristics of GaN is by the introduction of optically-active impurities (such as rare-earth elements) by ion implantation. Ion implantation has a twofold effect on the optical characteristics of GaN, by introducing lattice defects as well as optically active impurities. The effects of implantation-produced lattice defects on the optical characteristics of GaN are particularly important to understand if applications are to be exploited.

Most of the luminescence studies of ion implanted GaN reported in the literature have been directed towards three main purposes.

1. To study the effects of ion-beam-produced lattice defects on luminescence (i.e. appearance of new luminescent peaks due to defects or quenching of the characteristic luminescence peaks exhibited by as-grown GaN due to the introduction of competitive recombination centers).
2. To study the effects of implanted species (such as potential contaminants or rare-earth elements).
3. To monitor recovery of ion-beam-produced damage by post-implantation annealing.

Below, we discuss mainly the influence of implantation damage on the luminescence of GaN, which has been studied in [1–5,16,17,20,23,30,68–70,76,79–83,85–87,106–110]. We will not discuss rare-earth doping of GaN by ion implantation because this subject has been reviewed in detail elsewhere [1,5].

7.1. The effect of implantation disorder on light absorption

Implantation-produced damage significantly changes the absorption of visible light in GaN. Indeed, as-implanted GaN grown on sapphire undergoes color changes from yellowish-brown to black, depending on ion dose or the amount of implantation-produced damage. This fact suggests that implantation-induced defects act as strong absorbers of light in the blue part of the visible spectrum. Silkowski et al. [83] studied the RT absorption edge of GaN bombarded with 390 keV Ar ions to a dose of 5×10^{15} cm^{-2} and subsequently annealed at temperatures from 800 to 1050°C in flowing NH_3 or N_2 gas. Their data has shown that implantation damage results in an exponential tail of states near the band-edge. It is surprising that, despite the importance of this problem, more detailed studies of the influence of implantation-produced defects on light absorption have not been carried out.

7.2. Quenching of luminescence by ion implantation

All photoluminescence (PL) and cathodoluminescence (CL) data from ion implanted GaN shows that implantation-produced lattice defects act as effective non-radiative recombination centers in GaN, resulting in a severe quenching of most characteristic luminescence peaks exhibited by as-grown GaN. For example, Fig. 31(a) shows CL spectra obtained at RT from virgin and implanted regions of GaN bombarded with 150 keV C ions at LN_2 to a dose of 1×10^{14} cm^{-2}. The spectra

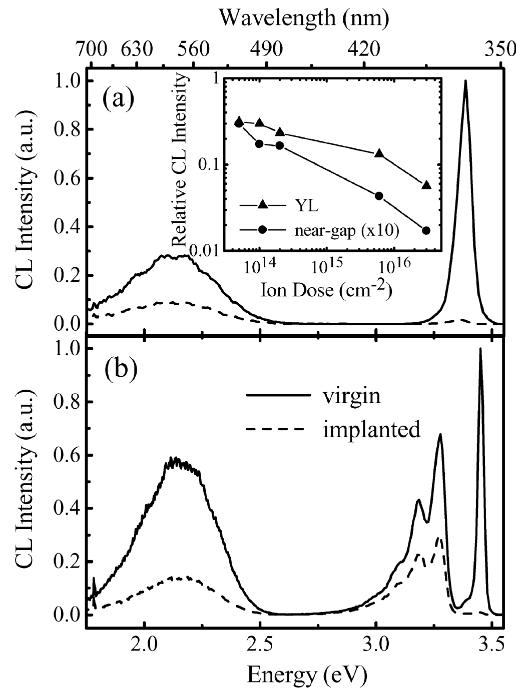

Fig. 31. CL spectra obtained at RT (a) and LN_2 (b) from virgin and implanted regions of GaN bombarded with 150 keV C ions at LN_2 with a beam flux of 3.4×10^{13} cm^{-2} s^{-1} to a dose of 10^{14} cm^{-2} (electron beam energy = 20 keV, CL bandpass = 2.5 nm for (a) it is 1.25 nm for (b)). The inset in (a) illustrates the ion dose dependence of the intensities of near-gap and yellow luminescence peaks measured at RT from implanted parts of the samples relative to the corresponding CL intensities in the virgin parts of these samples.

illustrate the effect of implantation-produced quenching of the intensities of both near-gap emission (centered on ~3.39 eV) and the yellow luminescence (YL) band (a broad defect- and/or impurity-related peak centered on ~2.12 eV) present in this GaN wafer. The inset in Fig. 31(a) shows the ion dose dependence of the intensities of near-gap and YL peaks at RT in implanted parts of samples relative to the corresponding CL intensities in the virgin parts of these samples. It is seen that, with increasing dose of 150 keV C ions, the intensities of both near-gap and YL peaks are drastically reduced.

Fig. 31(b) shows CL spectra obtained at LN_2 from virgin and implanted regions of a GaN sample implanted under the same conditions as the sample shown in Fig. 31(a). The LN_2 spectra in Fig. 31(b) consist of near-gap emission at 3.45 eV; donor–acceptor pair (DAP) emission at 3.28 eV with two LO phonon replicas at 3.18 and 3.08 eV, respectively [111]; a broad YL band centered on 2.16 eV; and the sharp: Al_2O_3 emission from the substrate at 1.78 eV. The ripples visible in the YL band in Fig. 31 are due to the micro-cavity effect [112].

It is seen from Fig. 31(b) that ion implantation considerably reduces the intensities of all CL peaks present at LN_2 in the visible part of the spectrum. However, the intensity of near-gap emission is quenched more efficiently than that of the other CL peaks shown in Fig. 31(b). A similar effect can be seen from Fig. 31(a) for the case of RT CL data. Indeed, Fig. 31(a), as well as the inset in this figure, shows that ion implantation preferentially reduces the measured intensity of near-gap emission. The depth-resolved CL measurements discussed below will provide an explanation for this effect.

Fig. 32 shows near-gap and YL depth profiles obtained at RT from a GaN sample bombarded with 150 keV C ions at LN_2 to a dose of 5×10^{13} cm^{-2}. In such depth profiles, the CL intensity is

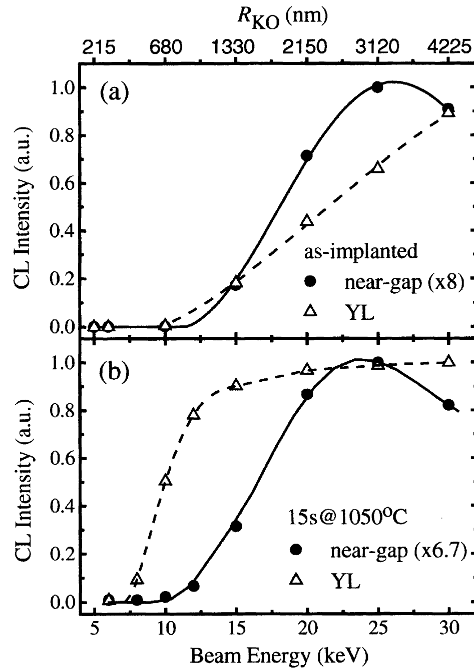

Fig. 32. Near-gap and yellow luminescence (YL) depth profiles obtained at RT from a GaN sample bombarded with 150 keV C ions at LN_2 with a beam flux of 3.4×10^{13} cm^{-2} s^{-1} to a dose of 5×10^{13} cm^{-2} (CL bandpass = 25 nm, electron beam power = 7 μW). Shown are the depth profiles of the implanted GaN sample before (a) and after (b) post-implantation annealing at 1050°C for 15 s.

plotted as a function of electron beam energy or the corresponding electron penetration range, R_{KO}, which can be approximated using the Kanaya–Okayama equation [113].

Fig. 32(a) shows that, in the ion-damaged layer (up to ~700 nm from the surface), the intensities of both near-gap and YL peaks are drastically reduced below the detectable level. Therefore, CL emission from the implanted sample shown in Fig. 31, obtained with an electron beam energy of 20 keV, is actually generated by the electron beam impinging on virgin GaN, beyond the implanted layer[8]. This observation can be used to explain the preferential quenching of near-gap emission compared with the other emission peaks in Fig. 31. Indeed, it has been shown [114] that self-absorption can change detected CL near-gap emission of as-grown GaN. Results from [91] also indicate that implantation-induced absorption of CL in the implanted layer can strongly affect detected near-gap emission from underlying virgin GaN. Note that, in as-grown GaN, the measured intensity of near-gap emission decreases with increasing electron beam energy due to efficient self-absorption, and the YL intensity increases with beam energy due to a corresponding increase in the concentration of YL centers towards the GaN/sapphire interface (see for example, [114]) and/or due to the saturation of YL emission.

As has been reported by several groups (see for example [23,70,79,80,83,85]), the annealing of GaN implanted with keV ions usually recovers (although always only partly) the measured intensities of light emission. Such partial recovery of luminescence intensity is generally attributed

[8] Note that the sample shown in Fig. 28 was bombarded to twice the dose (1×10^{14} cm^{-2}) of the sample shown in Fig. 29 (5×10^{13} cm^{-2}). Therefore, the effect of the quenching of CL emission coming from the implanted layer is even more pronounced in Fig. 28.

to a corresponding partial recovery of non-radiative defects produced by ion bombardment. However, as reported in [90], implantation-produced damage and post-implantation annealing affect not only light emission from the implanted layer but also the detection of CL emission from virgin GaN due to the absorption of light within the implanted layer. Awareness of this behavior is required for a correct interpretation of luminescence measurements of GaN optically doped by implantation with keV ions.

Shown in Fig. 32(b) are CL depth profiles taken from the same sample shown in Fig. 32(a) after annealing at 1050°C for 15 s. It is seen that such an annealing does not recover either near-gap or YL emission generated in the near-surface region (up to ~450 nm from the surface). This depth is consistent with TRIM calculations [11], which indicate that the layer directly modified by bombardment with 150 keV C ions (say, $R_p + 3\Delta R_p$, where R_p is the projected ion range, and ΔR_p is the ion straggling) is also ~450 nm thick. Therefore, the apparent recovery of emission by such an annealing[9] can be attributed to the thermal recovery of damage that enhances the absorption of light within the implanted layer. This conclusion is consistent with changes in the color of implanted samples observed to result from annealing [90]. Results from [90] have shown that the (partial) recovery of CL emission in the implanted layer by annealing at temperatures up to 1050°C occurs only for rather low dose implantation with 150 keV C ions (doses of $\sim 10^{12}$ cm^{-2}).

Another interesting result from Fig. 32(a) is that, in as-implanted GaN, the CL is quenched up to a depth of ~700 mm, which is well beyond the layer modified by ion bombardment, as given by TRIM [11], which takes into account only collisional processes. Such quenching of CL emission beyond the ion penetration range can be attributed to the diffusion of implantation-produced point defects. This conclusion is supported by the fact that ion-generated point defects are highly mobile in GaN at LN_2 and above. Fig. 32(b) also shows that the defect complexes formed by such mobile point defects can be effectively removed by annealing at 1050°C.

The conclusion that CL of GaN is dramatically quenched by relatively low dose ion bombardment is consistent with the results of luminescence studies of GaN irradiated with MeV light ions [30,115]. An analysis of CL spectra from GaN implanted with 150 keV C or 1.8 MeV He ions at RT has shown that disorder produced by light-ion bombardment to a critical dose corresponding to the generation of $\sim 5 \times 10^{19}$ vacancies per centimetercube is sufficient to reduce the intensity of near-gap emission by more than two orders of magnitude [90]. However, the exact value of this critical dose depends on a number of implant parameters, such as ion mass, energy, beam flux, and substrate temperature [115].

7.3. New luminescence peaks

It can be concluded that implantation-produced lattice defects themselves (both before and after post-implantation annealing of GaN) do not give rise to any luminescence peaks in the visible part of the spectrum. Although, the first reports on PL of ion implanted GaN suggested that implantation disorder was responsible for YL in GaN [79,80,116], this conclusion has not been supported by later experiments. Indeed, luminescence data from more recent reports suggests that YL originates from a defect-impurity complex [83,85,115]. The impurities which are responsible for YL are still unknown, although some results support carbon and oxygen as plausible candidates [83,115–117].

[9] After such an annealing of the sample from Fig. 32, the relative intensity of near-gap emission (measured with an electron beam energy of 20 keV) in the implanted part to that in the virgin part of the sample recovered from ~4% in the as-implanted sample to ~14% in the annealed one.

Another luminescence peak which has been attributed to implantation-produced defects is a peak centered on ~3.41 eV (at 4 K) [107]. However, this peak also cannot be attributed to implantation-produced defects alone since it is usually present after implantation in only selected GaN wafers. Therefore, this peak is more likely related to a defect-impurity complex, rather than to some structural defects alone.

Implantation defects produced by proton bombardment of GaN have been shown to give rise to a broad infrared PL band centered on ~0.95 eV [118–120]. A similar band, attributed to lattice defects, has been reported for GaN irradiated with MeV electrons [3,4,5]. However, the nature of defects responsible for this band is still unknown.

8. Electrical characteristics

8.1. Doping with donor species (Si, O, S, Se, and Te)

Most of the n-type doping in GaN by ion implantation has been performed with Si implants. Fig. 33 shows the sheet resistance of initially resistive GaN after Si^+ or Mg^+ implantation as a function of annealing temperature. At temperatures above 1050°C, Si becomes electrically active, producing a sharp decrease in resistivity [121]. Variable temperature Hall measurements showed the ionization level to be ~30–60 meV. Subsequently, ion channeling, nuclear reaction analysis, and particle-induced X-ray emission measurements have shown that almost 100% of the Si goes onto the Ga site at 1100°C [73], creating the shallow donor state (see Section 6.4).

Fig. 34 shows the sheet electron concentration in Si-implanted GaN for 1100°C annealing as a function of implant dose [84]. For the two highest dose Si-implanted samples (5 and 10×10^{15} cm^{-2}), 35% and 50%, respectively, of the implanted Si ions create ionized donors at RT [85]. The possibility that implant damage alone is generating the free electrons can be ruled out by comparing the Ar- and Si-implanted samples at the same dose, the latter exhibiting over a factor of 100 more free electrons. If implantation damage was responsible for the carrier generation or for enhanced conduction by a hopping mechanism, then the Ar-implanted samples, as a result of Ar's heavier mass, would have demonstrated at least as high a concentration of free electrons as the Si-implanted sample. Since this is not the case, implant damage cannot be the cause of the enhanced

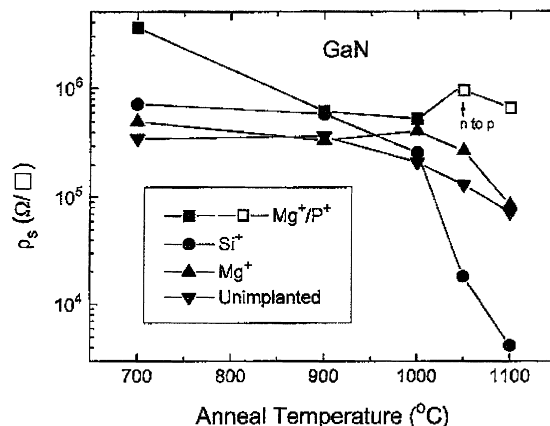

Fig. 33. Sheet resistivity in Si, Mg and Mg/P implanted GaN, as a function of annealing temperature. The implant dose was 10^{14} cm^{-2} at an energy of 100 keV in each case.

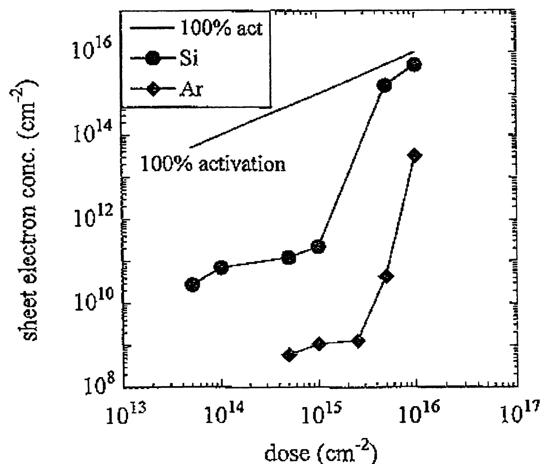

Fig. 34. Sheet electron density vs. implantation dose of each ion for Si- and Ar-implanted GaN annealed at 1100°C for 15 s. The top line represents 100% activation of the implanted dose assuming full ionization.

conduction, and the implanted Si must be activated as donors. The significant activation of the implanted Si in the high-dose samples and not the lower-dose samples was attributed to the need for the Si concentration to exceed the background carbon concentration ($\sim 5 \times 10^{18}$ cm^{-3}) that was thought to be compensating the lower-dose Si samples [84].

Oxygen implantation also creates n-type doping in GaN [94]. Fig. 35 shows an Arrhenius plot of the sheet resistivity of GaN before and after O^+ implantation and 1100°C annealing. The oxygen creates a shallow donor state with an activation energy of 29 meV, but there is relatively low efficiency; i.e. $\leq$10% of the implanted oxygen becomes electrically active.

Fig. 36 shows an Arrhenius plot of S^+ activation in GaN [92]. The sheet carrier concentration measured at 25°C shows an activation energy of 3.16 eV for the annealing temperature range between 1000 and 1200°C and basically saturates thereafter. The maximum sheet electron density, $\sim 7 \times 10^{13}$ cm^{-2}, corresponds to a peak volume density of $\sim 5 \times 10^{18}$ cm^{-3}. This is well below that achieved with Si^+ implantation and annealing ($>10^{20}$ cm^{-3}) [91,95,122,123]. In the latter case, the

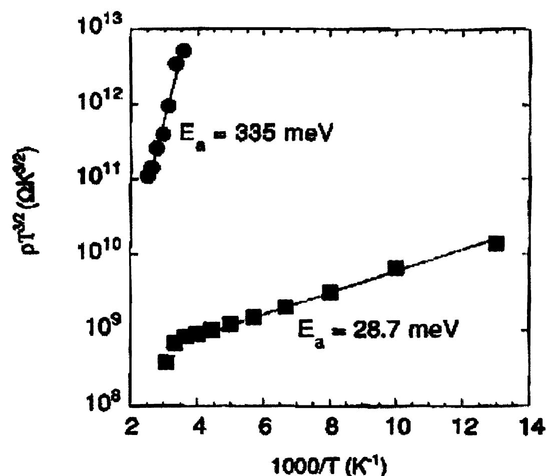

Fig. 35. Arrhenius plot of sheet resistivity of GaN before and after O^+ implantation.

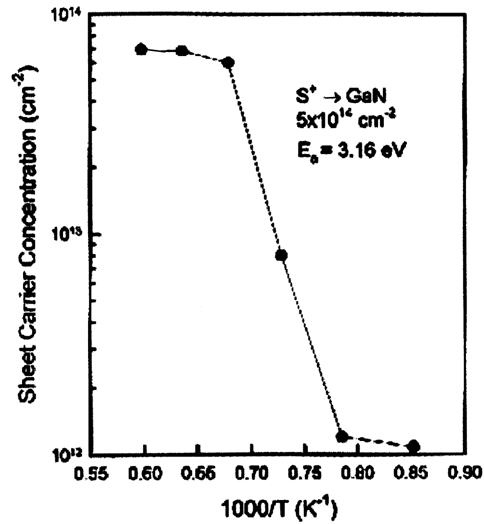

Fig. 36. Arrhenius plot of sheet electron density in S^+-implanted GaN vs. annealing temperature.

carrier density showed an activation energy of 5.2 eV. The physical origin of this activation energy contains several components — basically it is the energy required to move an implanted ion onto a substitutional lattice site and for it to show electrical activity. This latter requirement means that compensating defects must also be annealed out. Even though implanted Si at the same dose showed evidence of site switching and self-compensation [95], it still produces a higher peak doping level than the non-amphoteric donor S, which is only slightly heavier (^{32}S versus ^{28}Si). From temperature-dependent Hall measurements, we find a S^+ donor ionization level of 48 ± 10 meV, so that the donors are fully ionized at RT [92].

Similar data is shown in Fig. 37 for Te^+ implantation. The activation starts around the same temperature as for S, but much lower sheet electron densities are obtained, the activation energy is

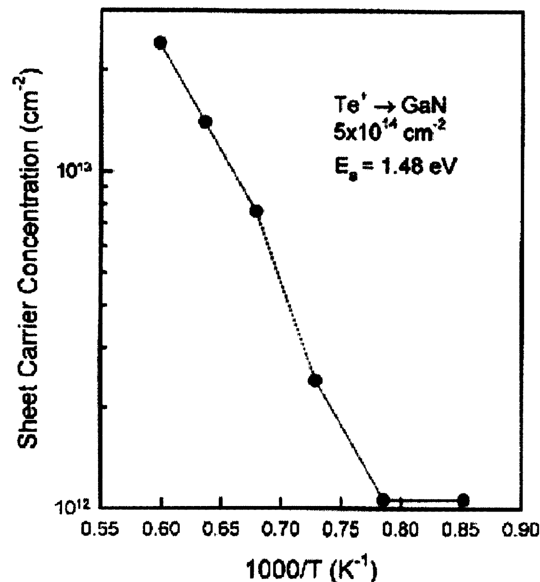

Fig. 37. Arrhenius plot of sheet electron density in Te^+-implanted GaN vs. annealing temperature.

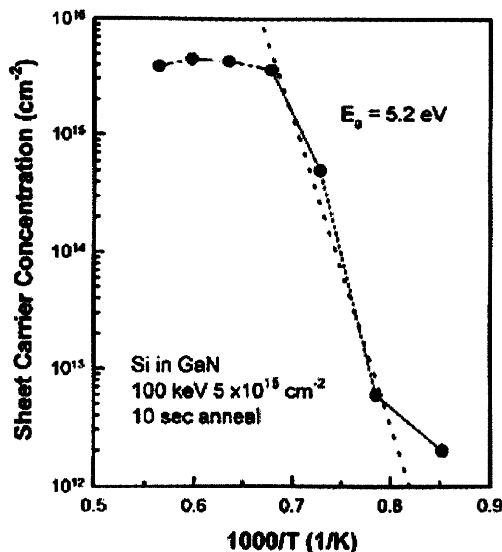

Fig. 38. Arrhenius plot of sheet electron density in Si^+-implanted GaN vs. annealing temperature.

significantly lower (1.5 eV), and the carrier concentration does not saturate, even at 1400°C. It is likely that because of the much greater atomic weight of ^{128}Te, even higher annealing temperatures would be required to remove all its associated lattice damage, and that the activation characteristics are still being dominated by this defect removal process. Residual lattice damage from implantation is electrically active in all III–V semiconductors, producing either high resistance behavior (GaAs) or residual n-type conductivity (InP, GaN). The only data available on group VI doping in epitaxial material are from Se-doped MOCVD material, where maximum electron concentrations of 2×10^{18} to 6×10^{19} cm^{-3} were achieved [103,124]. These are also below the values reported for Si doping, suggesting that the group VI donors do not have any advantage over Si for creation of n-type layers in GaN. From limited temperature-dependent Hall data, the Te ionization level was estimated to be 50 ± 20 meV [92].

Data for activation of Si^+ implants in GaN is shown in Fig. 38. The activation energy of 5.2 eV is higher than that for the group VI dopants discussed above, but overall Si is the best choice for creating n-type doping in GaN.

AlGaN layers will be employed in heterostructure transistors to realize a two dimensional electron gas (2-DEG) and to increase the transistor breakdown voltage. Implantation can be used to reduce the transistor access resistance of the AlGaN barrier. One would anticipate that the addition of Al to the GaN matrix will increase the damage threshold as is the case for AlGaAs as compared to GaAs [125], but little work has been reported in this area. Recently the first implantation doping studies have been reported for AlGaN [104,127].

Zolper et al. [126] used AlGaN layers nominally 1.0 μm thick grown on *c*-plane sapphire substrate for Si implantation studies. The Al composition was estimated to be ~15% based on X-ray and PL measurements. The minimum RBS/C yield in these samples was 2.0%, comparable to high quality GaN layers. The AlGaN samples were implanted with 100 keV Si at RT at one of two doses, 1 or 5×10^{15} cm^{-2}. Fig. 39 shows the sheet electron concentration versus the annealing temperature for the Si-implanted AlGaN sample. Data for an unimplanted sample is included as a control. First of all, it is clear that the unimplanted samples have significant donors produced by the annealing process alone. This may be due to the activation of unintentional impurities, such as Si or O, in the

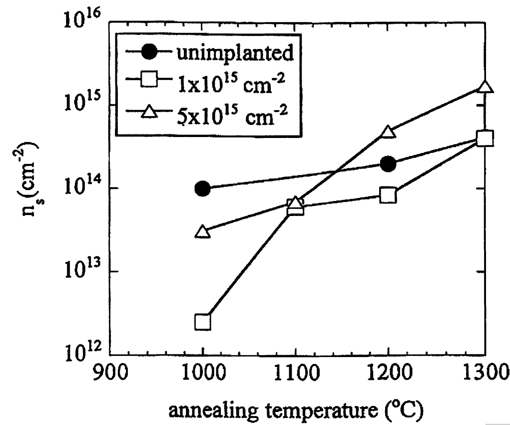

Fig. 39. Sheet electron concentration for unimplanted and Si-implanted (100 keV) AlGaN (15% AlN) at the doses shown vs. annealing temperature.

film. O may be a particular suspect due to the tendency of O to incorporate in an Al-containing material. At the highest temperature, the high dose Si-implanted sample has four times higher free electron concentration (1.7×10^{15} cm^{-2}) than the unimplanted sample. This corresponds to 34% activation of the implanted Si.

8.2. Doping with acceptor species

In Fig. 33 we had also shown activation data for Mg and Mg/P implanted GaN. The purpose of the co-implant scheme is to enhance occupation of Ga substitutional sites by the group II acceptor Mg. An n-to-p conversion was observed after 1050°C annealing, corresponding to movement of the Mg atom onto substitutional sites.

Similar results were observed for Ca and Ca/P implanted GaN [94], as shown in Fig. 40. The n-to-p conversion occurred at 1100°C, and the p-type material showed an activation energy of

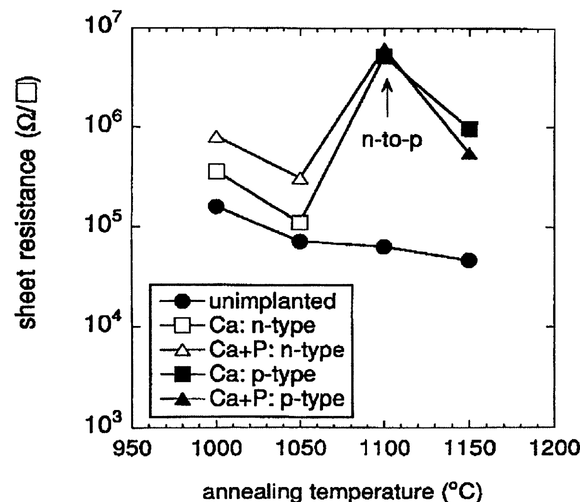

Fig. 40. Sheet resistivity in Ca or Ca/P implanted GaN, as a function of annealing temperature. The implant dose was 10^{14} cm^{-2} at an energy of 100 keV in each case.

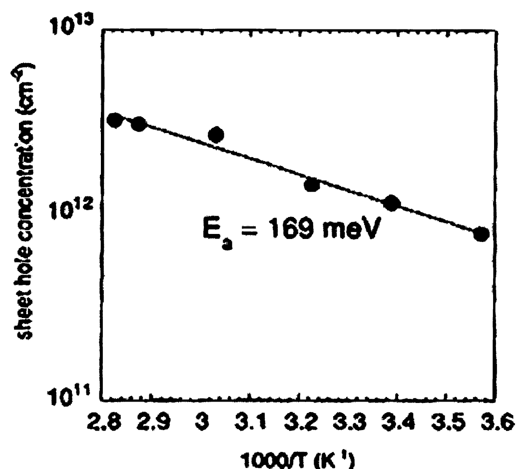

Fig. 41. Arrhenius plot of activation energy of implanted Ca acceptors in GaN.

~169 meV for the Ca acceptor (Fig. 41). Ion channeling results found that 80% of the Ca was near Ga sites as-implanted, with a displacement of ~0.2 Å from the exact Ga site. Upon annealing at 1100°C, the Ca moved onto the substitutional Ga lattice positions [74] (see Section 6.4).

The effects of post-implant annealing temperature on the sheet carrier concentrations in Mg^+ and C^+ implanted GaN are shown in Fig. 42 [92]. There are two important features of the data: (i) we did not achieve p-type conductivity with carbon, and (ii) only ~1% of the Mg is electrically active at 25°C. Carbon has been predicted previously to have a strong self-compensation effect [127], and it has been found to produce p-type conductivity only in metalorganic molecular beam epitaxy where its incorporation on a N-site is favorable [128]. Based on an ionization level of ~170 meV, the hole density in Mg-doped GaN would be calculated to be ~10% of the Mg acceptor concentration when measured at 25°C. In [92], the number of holes was an order of magnitude less than predicted. This

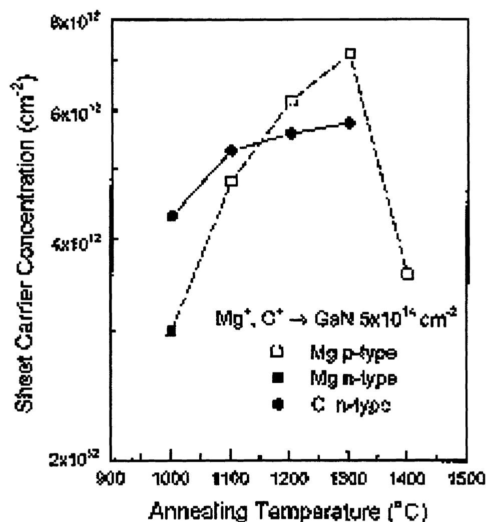

Fig. 42. Sheet carrier densities in Mg^+- or C^+-implanted GaN as a function of annealing temperature.

Table 8
Characteristics of different dopants implanted into GaN

	Max achievable doping level (cm^{-3})	Diffusivity ($cm^2 s^{-1}$)	Ionization level (meV)
Donors			
Si	5×10^{20}	$<2 \times 10^{-13}$ (1500°C)	28
S	5×10^{18}	$<2 \times 10^{-13}$ (1400°C)	48
Se	2×10^{18}	$<2 \times 10^{-13}$ (1450°C)	–
Te	1×10^{18}	$<2 \times 10^{-13}$ (1450°C)	50
O	3×10^{18}	$<2 \times 10^{-13}$ (1200°C)	30
Acceptors			
Mg	$\sim 5 \times 10^{18}$[a]	$<2 \times 10^{-13}$ (1450°C)	170
Ca	$\sim 5 \times 10^{18}$[a]	$<2 \times 10^{-13}$ (1450°C)	165
Be	$<5 \times 10^{17}$	Defect-assisted	–
C	n-type	$<2 \times 10^{-13}$ (1400°C)	–

[a] Acceptor concentration.

should be related to the existing n-type carrier background in the material. At the highest annealing temperature (1400°C), the hole density falls, which could be due to Mg coming out of the solution or to the creation of further compensating defects in GaN [92].

We also point out that, unless most residual defects are removed by annealing, the implanted acceptors will remain compensated and not create p-type material [129,130]. Improved optical activation of Zn acceptors in implanted GaN has been achieved using annealing under a high overpressure (10 kbar) of N_2 [131,132].

Theoretical evidence suggests that Be may be an effective acceptor in GaN when co-incorporated with oxygen [133]. Be solubility in GaN is predicted to be low due to the formation of Be_3N_2, but co-incorporation might enhance the solubility. There have been some experimental indications of such a result [134], but these have not been verified.

Table 8 summarizes the current level of understanding of maximum achievable doping levels, ionization energies, and diffusivities for species implanted into GaN. It appears that Si is the best choice for n-doping, while either Mg or Ca are the best choices for p-type doping.

8.3. Implantation-produced deep levels

In this section, we briefly summarize the results of DLTS studies of electron or ion irradiated GaN [135–144]. Table 9 gives the energy levels of the deep traps identified in ion implanted GaN. Several additional deep traps have been found to form in GaN during sputter deposition of contacts due the introduction of lattice defects by this process (see [138–140] for details).

Table 9
Deep traps in ion implanted GaN, as identified by DLTS[a]

Implant	Energy level (eV)	Label	Reference
5.4 MeV ^4He	0.95 ± 0.05	ER5	[135]
5.4 MeV ^4He	0.78 ± 0.05	ER4	[135]
5.4 MeV ^4He	0.20 ± 0.01	ER3	[137]
2 MeV ^1H	0.16 ± 0.03	ER2	[136]
2 MeV ^1H	0.20 ± 0.01	ER3	[136]
2 MeV ^1H	0.13 ± 0.01	ER1	[136]
0.27 MeV ^{14}N	0.67 ± 0.02	D3	[141]

[a] Given are energy levels below the conduction band.

It should also be noted that deep traps identified in DLTS studies discussed here most likely originate from some defect complexes (or impurity-defect complexes) in GaN rather than from simple point defects, such as vacancies and interstitials. Indeed, results of a number of recent studies [33,145,146] strongly suggest that ion-produced Frenkel pairs are mobile in GaN at RT.

8.4. Isolation

Implant isolation has been widely used in compound semiconductor devices for inter-device isolation such as in transistor circuits or to produce current confinement such as in lasers [147–149]. The implantation process can compensate a semiconductor layer either by a damage or chemical mechanism. For damage compensation, the resistance typically goes through a maximum with increasing post-implantation annealing temperature as damage is annealed out and hopping conduction is reduced. At higher temperatures, the defect density is further reduced below that required to compensate the material, and the resistivity decreases. For chemical compensation, the post-implantation resistance again increases with annealing temperature with a reduction in hopping conduction but it then stabilizes at higher temperatures as a thermally stable compensating deep level is formed. Typically, there is a minimum dose (dependent on the doping level of the sample) required for the chemically active isolation species to achieve thermally stable compensation [150]. Thermally stable implant isolation has been reported for n- and p-type AlGaAs where an Al–O complex is thought to form [150,151] and for C-doped GaAs and AlGaAs [152]. With this background, the implant isolation properties of the III-N materials are reviewed.

A number of studies of electrical isolation of GaN have been reported in the literature [87,121,153–157]. It has been shown that isolation which withstands thermal annealing at temperatures at least up to 500°C can be readily achieved by irradiation of GaN with keV H, He, N, O, Ti, Cr, or Fe ions. For example, Fig. 43 shows that N-implantation (at doses of 10^{12}–10^{13} cm^{-3}) effectively compensates both p- and n-type GaN [121]. For both doping types, the resistance first increases with annealing temperature and then reaches a maximum before demonstrating a significant reduction after an 850°C anneal for n-type and a 950°C anneal for p-type GaN. This behavior is typical for implant-damage compensation. The defect levels estimated from Arrhenius plots of the resistance/temperature product are 0.83 eV for initially n-type and 0.90 eV for initially

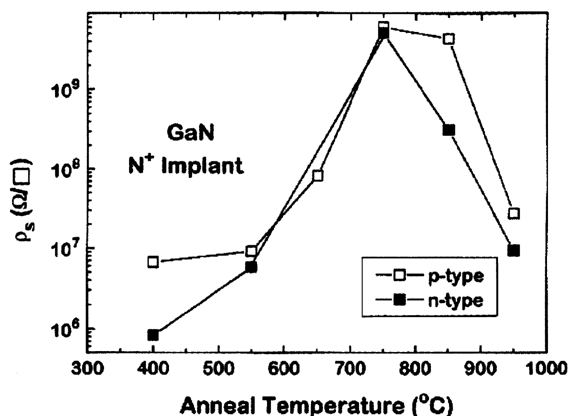

Fig. 43. Sheet resistance vs. annealing temperature for N implanted initially n- and p-type GaN. The N was implanted at multiple energies to give an approximately uniform ion concentration of 4×10^{18} cm^{-3} across ~500 nm.

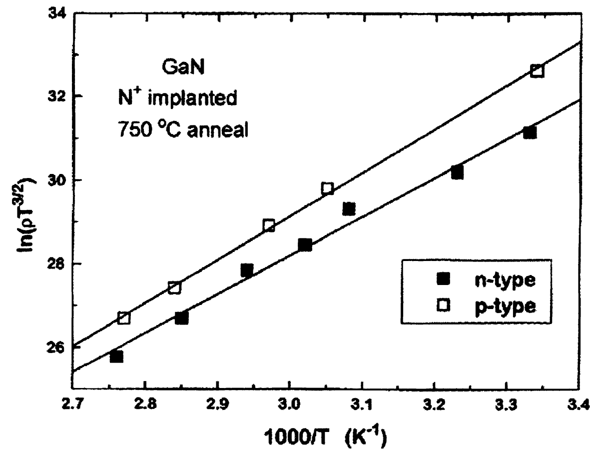

Fig. 44. Arrhenius plots of sheet resistance in N^+-implanted n- and p-GaN annealed at 750°C.

p-type GaN (Fig. 44). These levels are still not at mid-gap but are sufficiently deep to realize a sheet resistance of $>10^9\ \Omega\ sq^{-1}$.

As has been reported by several groups [121,153,154], implant isolation in GaN can be stable to RTA at temperatures up to 800–900°C. However, H-implanted compensation of n-type GaN has been reported to anneal out at ~400°C with an anomalous dependence on implant energy. The reason for this is presently not known. Moreover, electrical isolation of GaN appears to rely solely on implantation damage without any chemical compensation effects analogous to those in the AlGaAs/GaAs case. Further work is still required to understand the electrical nature of implantation damage in GaN.

Most of isolation studies in GaN reported in the literature have been done using keV ion implantation [87,121,153–156]. However, in the case of keV ion implantation, the implanted species stop inside the conductive GaN layer, and the damage profile is highly non-uniform throughout the GaN film. This makes the separation of the effects of defect and chemical isolation (and, therefore, the interpretation of data) difficult. Another problem of electrical isolation by keV ion bombardment is that many GaN-based devices are fabricated from quite thick ($\geq$1.5 μm) GaN epilayers. In this case, the achievement of adequate electrical isolation using conventional keV ion bombardment requires a large number of overlapping implants, which is undesirable.

To overcome the problems of electrical isolation of GaN with keV ions, MeV light ion irradiation has been applied [157]. In this case, projected ion ranges are greater than the thickness of typical GaN epilayers, and the profiles of generated atomic displacements are essentially uniform throughout the conductive GaN film. A single MeV implant, therefore, is sufficient to isolate a relatively thick GaN film. Moreover, irradiation with MeV ions allows effects of defect isolation to be separated from chemical isolation and to avoid the formation of a layer with substantial defect-induced (hopping) conduction, which inevitably forms at the ion end-of-range region in the case of keV implants and usually complicates the interpretation of data (see for example [147]).

Fig. 45(a) shows the evolution of sheet resistance (R_s) of resistors with different original free electron concentrations (n) exposed to irradiation with 6.6 MeV C ions at RT [157]. This figure reveals that each of the curves has three distinct dose regions. The first region comprises the lowest doses, where R_s increases only slightly with increasing ion dose. The second region is characterized by a very fast increase in the value of R_s (by 9–10 orders of magnitude) in a relatively narrow dose interval. Such an increase in R_s is caused by the trapping of carriers at defects created by ion

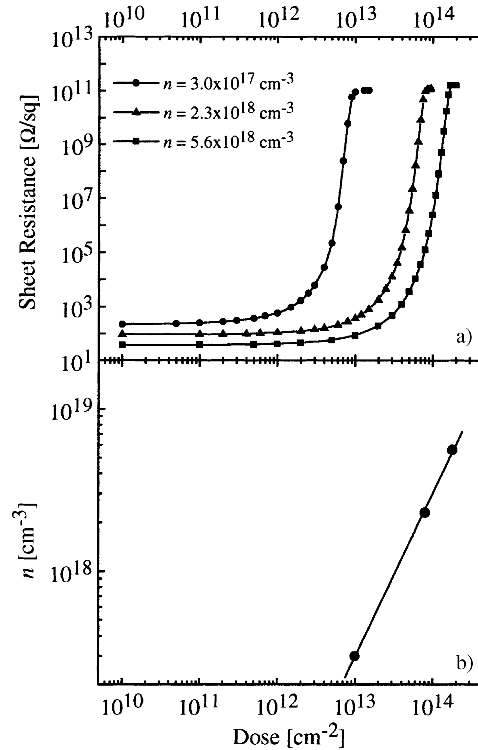

Fig. 45. (a) Dose dependence of sheet resistance of GaN samples irradiated with 6.6 MeV C ions. Samples had different original free electron concentrations, as indicated in the legend. (b) The original free carrier concentration of the samples vs. threshold doses obtained from data in (a). The straight line with a slope of 1.0, representing the best fit, is shown.

irradiation and damage-induced degradation of carrier mobility. Fig. 45(a) also shows that, with further increasing ion dose, R_s values reach their highest levels after a certain dose has been accumulated (D_{th}: the so-called threshold dose). The third dose region is for ion doses larger than D_{th}. With increasing ion dose above D_{th} and up to the maximum doses used in [157], the measured values of R_s remain approximately constant, forming a plateau. The levels of R_s at the plateaus shown in Fig. 45 are of the order of $1–2 \times 10^{11}\ \Omega\ sq^{-1}$. However, the real maximum values of R_s of GaN layers are even larger since the R_s values measured have a contribution from the parasitic resistances of the experimental set-up, which are of the same order of magnitude [157].

Fig. 45(a) clearly shows that the dose dependence of R_s is not linear. A similar non-linear dose dependence in GaN has previously been observed and explained by Uzan-Saguy et al. [87] based on a theory of electron transport in doped poly-crystalline materials. However, this non-linearity of R_s as a function of ion dose may be more simply explained. Indeed, in the first approximation, the concentration of deep traps, created by ion irradiation, linearly increases with dose, and, consequently, n will linearly decrease with ion dose. Therefore, the strong non-linear dose dependence of R_s observed in Fig. 45(a) is not unexpected, taking into account that $R_s \propto 1/n$. Moreover, with increasing number of traps in GaN, the concentration of charged scattering centers significantly increases, and electron mobility decreases, contributing to strong non-linearity of R_s on ion dose. In addition, the real dose dependence of R_s may be more complex. For example, the concentration of deep traps may not increase linearly with dose due to complex defect interaction and dynamic annealing processes, as discussed in detail in Section 2.

In Fig. 45(b), the threshold doses of C ions [taken from Fig. 45(a)] are plotted versus the values of original free carrier concentration. Also shown in this figure is a straight line fit with a slope of 1.0, which shows that D_{th} increases linearly with the original concentration of free carriers. This result may support (despite the complexity of the real defect processes taking place in GaN during ion bombardment) the above assumption that the dose dependence of n has a form of $n(D) = n(0) - AD$, where D is ion dose, $n(D)$ is free carrier concentration in the conductive layer after bombardment to dose D, and A is a constant which depends on ion mass and energy.

Fig. 46(a) shows the evolution of R_s in identical resistors irradiated with 0.6 MeV H, 3.0 MeV Li, 6.6 MeV C, and 6.6 MeV O ions at RT [157]. It is seen that the curves progressively shift towards lower doses with increasing ion mass. This fact is related to the creation of a higher defect concentration in the conductive layer in the case of higher ion masses. In all the samples studied, R_s values reach their highest levels after D_{th} has been accumulated. Plotted in Fig. 46(b) is the number of atomic displacements (calculated using the TRIM code [11]) produced by the above four ion species in the conductive GaN layer versus the threshold doses. A straight line fit (with a slope of -1.0) shown in Fig. 46(b) demonstrates that the efficiency of carrier removal processes reciprocally depends on the number of atomic displacements.

The above results show that ion doses required for an effective isolation of GaN have simple linear and reciprocal dependencies on the values of initial free carrier concentration and ion-beam-produced atomic displacements, respectively. As a result, implant conditions necessary for an effective electrical isolation of a particular GaN-based device can be readily estimated based on experimental data reported in [157] and the number of atomic displacements calculated using, for

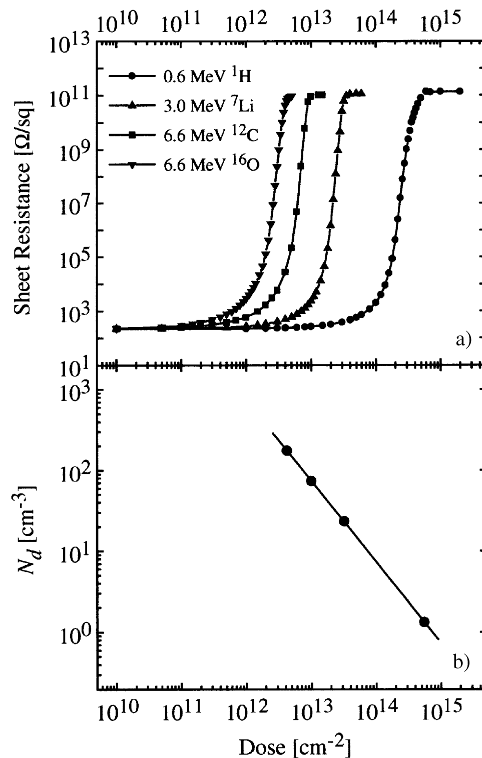

Fig. 46. (a) Dose dependence of sheet resistance in identical samples ($n = 3 \times 10^{17}$ cm^{-3}) for irradiation with different ions, as indicated in the legend. (b) The estimated concentration of atomic displacements (N_d) is plotted vs. threshold doses obtained from data in (a). Also shown is a straight line with a slope -1.0 which represents the best fit to experimental data.

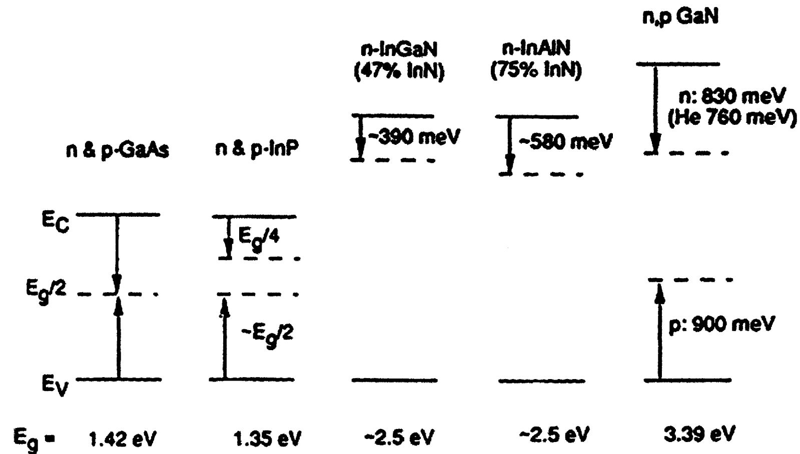

Fig. 47. Schematic representation of the position in the energy gap of compensating defect levels from implant isolation in GaAs, InP, $In_{0.47}Ga_{0.53}N$, $In_{0.75}Al_{0.25}N$ and GaN.

example, the TRIM code [11]. The technological application of ion bombardment for electrical isolation of GaN based devices is also facilitated by very high thermal stability of such isolation. Indeed, the samples irradiated to doses above D_{th} remain highly resistive after rapid thermal annealing at temperatures up to 900°C [157].

Very effective isolation of AlGaN/GaN heterostructure field effect transistor (HFET) structures has been achieved by Asbeck and co-workers using a combined P^+/He^+ implant process [158]. This study demonstrated that a dual energy (75/180 keV) P^+ implant (doses of 5×10^{11} and 2×10^{12} cm^{-2}, respectively) followed by a 75 keV He^+ implant (6×10^{13} cm^{-2}) was able to produce a sheet resistance of $\sim 10^{12}$ Ω sq^{-1} in AlGaN/GaN structures with 1 μm thick undoped GaN buffers. The temperature dependence of the resistivity showed an activation energy of 0.71 eV, consistent with previous measurements of deep states induced in GaN by implant damage [158].

Fig. 47 schematically summarizes the present knowledge of the position in the bandgap of the dominant compensating implanted defect levels in III-N materials and compares these to those in GaAs and InP. The present knowledge of deep traps in ion implanted GaN was briefly summarized in Section 8.3. Although the levels are not at mid-gap, as is ideal for optimum compensation in GaAs and p-type InP, with the exception of InGaN, they are sufficiently deep to produce high resistivity material.

In summary, electrical isolation of n- and p-type GaN can be done by ion irradiation. Results show that the sheet resistance of GaN layers can increase up to 1–2 $\times 10^{11}$ Ω sq^{-1} as a result of ion irradiation. The threshold dose (i.e. ion dose which is necessary to produce a concentration of effective deep level traps compared to the initial concentration of free carriers) linearly depends on initial free electron concentration and reciprocally depends on the number of atomic displacements produced in the GaN film.

9. Electronic devices

The best example of how ion implantation can directly impact the performance of group III-nitride transistors are illustrated in Fig. 48. The figure shows four device structures that could be employed to fabricate AlGaN/GaN high electron mobility transistors (HEMTs). To date, the majority

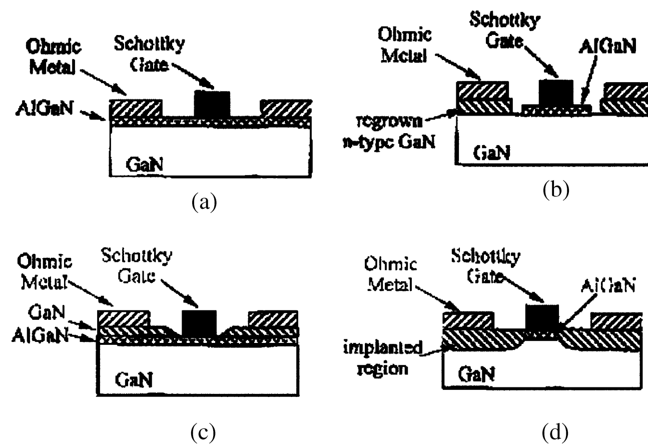

Fig. 48. Comparison of GaN-based HFET structures: (a) planar; (b) recessed gate; (c) regrown N^+ Ohmic regions; (d) self-aligned, implanted. Implantation is the most practical means to achieve the selective area doping required to reduce the transistor access resistance.

of the AlGaN/GaN HEMTs transistors have been fabricated in a planar structure as shown in Fig. 48(a), where the Ohmic source and drain contacts are placed directly on the wide bandgap AlGaN layer without any increased local doping to reduce the contact or access resistance. This leads to a high access resistance, reduced current capability, and a high transistor knee voltage, which in turn reduces the transistor power gain, power-added efficiency, and linearity. Fig. 48 (b) and (c) shows two approaches that have been taken to reduce the access resistance. One is to selectively etch away the wide bandgap material in the contact regions and then regrow highly doped GaN to improve access resistance; however, the manufacturability of this approach, as with any regrowth process, is questionable. The recess gate approach of Fig. 48(c) has been widely used in other mature compound semiconductors such as GaAs and InP. Although, this type of structure has been demonstrated in GaN-based devices, the unavailability of controlled wet etching of GaN requires the use of a plasma etch, which introduces surface damage in the semiconductor in the region under Schottky gate and degrades the rectifying properties of the gate. Finally, the self-aligned ion implanted structure of Fig. 48(d) is used to create selective areas of highly doped regions for the source and drain contacts in a highly manufacturable fashion without any plasma etching of the gate region. To date, ion implantation has been used to realize a GaN junction field effect transistor (JFET) but has not been applied to AlGaN/GaN HEMTs. One of the key challenges to applying ion implantation to AlGaN/GaN HEMTs is the avoidance of surface degradation that will negatively impact the Schottky gate formation during the high temperature implant activation anneal.

Progress in GaN-based electronics has been remarkably rapid due to several factors. One of these is that the experience gained in GaAs/AlGaAs HEMTs has been quickly applied to the GaN/AlGaN system. At one time it was thought that molecular beam epitaxy (MBE) and related techniques would be the best choice for growth of electronic device structures, and this may still be the case if GaN substrates become available. However for heteroepitaxial growth there is still a need to grow thick buffer structures grown using lateral epitaxical overgrowth (LEO), which are best done with MOCVD. The rapid advances in material purity, Ohmic contact quality and gate contact stability has fueled the progress in heterostructure field effect transistors (HFETs) in the GaN/AlGaN system. Much work remains to be done on vertical device structures such as thyristors and heterojunction bipolar transitions (HBTs), where minority carrier lifetime, interface quality and doping control are important factors. As with GaAs electronics, much of the impetus for nitride

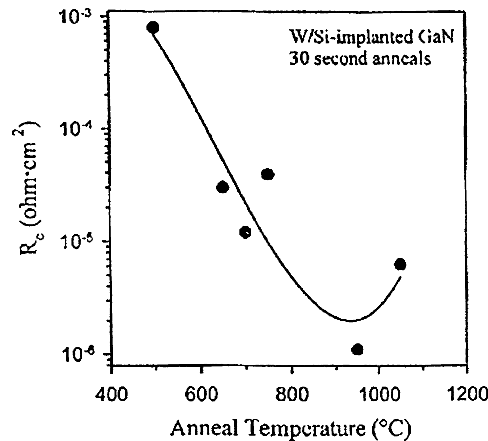

Fig. 49. Contact resistance vs. annealing temperature for W- on Si-implanted GaN that was initially activated at 1100°C to produce n^+ -GaN.

electronics is coming from defense applications and there is as yet no commercialization of these devices.

An example of how selective-area implantation can be used to improve Ohmic contact resistance on device structures is shown in Fig. 49 [159]. In this case, a W contact deposited on the implanted n-GaN showed minimum specific contact resistances of $\sim 10^{-4}\ \Omega\ \mathrm{cm}^2$. After implantation of Si^+ followed by activation at 1100°C to produce n^+ -GaN regions ($n \times 10^{20}\ \mathrm{cm}^{-3}$), subsequently deposited W contacts show a contact resistance almost 2 orders of magnitude lower than on unimplanted material.

10. Current problems

In this section, we briefly discuss current problems, mainly associated with implantation-produced disorder, which may hinder a successful application of ion implantation in the fabrication of GaN-based devices.

The main problem, which limits the application of ion implantation for doping and dry etching of GaN, is ion-beam-produced lattice disorder. Damage build-up studies, reviewed in Section 2, show that GaN is extremely resistant to ion-beam disordering. Indeed, very high ion doses are usually required to induce bulk amorphization of GaN due to very efficient dynamic annealing processes in this material compared to other semiconductors such as Si or GaAs. However, measurements of discrete defect levels and optical and electrical characteristics of ion implanted GaN, as reviewed in Sections 7 and 8, show that GaN is far from being resistant to ion beam disordering. Even relatively low dose implantation with light ions is sufficient to dramatically quench the intensity of all characteristic luminescent peaks of GaN due to the formation of lattice defects, which act as non-radiative recombination centers. Electrical properties of GaN are also very strongly modified by even relatively low dose implantation.[10] Therefore, even low dose implantation used for doping requires a post-implantation annealing step to remove ion-beam-produced defects detrimental for device performance.

[10] This fact has successfully been applied for electrical isolation of GaN by ion bombardment (see Section 8).

As discussed in Sections 6–8, annealing of implantation disorder in GaN faces difficulties. For example, luminescence studies have shown that annealing at temperatures up to $\sim$1100°C is not sufficient to completely remove implantation disorder produced in GaN even by very low dose light-ion bombardment (such as 10^{11} to 10^{12} cm^{-2} of 150 keV C ions). Annealing at higher temperatures is complicated by decomposition of GaN and generally requires capping of GaN surface with a protective layer as well as special RTA systems (see Section 6).

The problem of a satisfactory removal of implantation disorder becomes more difficult for higher dose ion implantation, which is desirable for p-type doping and Ohmic contact applications. High-dose ion implantation into GaN, under a wide range of implant conditions, results in the formation of extended defects within the implanted layer (see Section 2). It is well-known that extended defects in semiconductors are very resistive to annealing, requiring temperatures of roughly 2/3 of the melting point (or $\sim$1650°C for GaN). The formation of such extended defects may explain the well-known difficulties with post-implantation thermal annealing of ion beam damage in GaN.

Another technologically important issue is the ability to adequately recrystallize amorphous layers in ion bombarded GaN. Indeed, as discussed in Section 2, high-dose ion implantation of GaN often results in the formation of thick surface amorphous layers. In addition, a thin surface amorphous layer is often formed in GaN even during moderate-dose implantation due to the trapping of migrating point defects at the GaN surface. The formation of thin surface amorphous layers is also expected during dry etching owing to very high ion doses employed in this process. These amorphous layers in GaN represent a current problem due to the present inability to epitaxially recrystallize them. Results of studies discussed in Section 6 show that thermal annealing of amorphous GaN at temperatures above $\sim$500°C results in polycrystallization, rather than in solid phase epitaxial growth (i.e. layer-by-layer recrystallization of any amorphous phase). Annealing of amorphous layers is also complicated by thermally-induced decomposition at temperatures above $\sim$400°C. Such undesirable decomposition is related to ion-beam-induced porosity of GaN amorphized by ion bombardment. Unfortunately, amorphous and heavily disordered near-surface layers in GaN, the inevitable result of dry etching, cannot be removed by an annealing step. This explains why subsequent chemical removal of such damage has been necessary for device applications [40].

An obvious way to avoid high levels of undesirable ion-beam damage and, therefore, to suppress amorphization is elevated temperature implantation. However, elevated temperature ion bombardment is complicated by anomalous material erosion. In addition, both amorphous and heavily damaged layers of GaN exhibit anomalous material erosion during elevated temperature ion bombardment. This efficient erosion currently imposes significant limitations on the technological applications of ‘hot implants’ into GaN.

Despite the above problems of high-dose implantation, ion implantation to relatively low doses, followed by an annealing step, appears to be suitable for electrical isolation and selective-area doping of GaN-based electronic devices. However, an improved understanding of ion-beam-produced defects and their interactions is essential if ion implantation is to be fully utilized in the fabrication of GaN-based devices.

11. Concluding remarks

The current status of the field of ion implantation into GaN has been reviewed. Significant progress has been achieved for the past decade in the understanding of a number of important processes which occur during ion bombardment of GaN. However, compared to our understanding of

ion beam processes in mature semiconductors (i.e. Si and GaAs), the understanding of the complex ion-beam-induced processes in GaN is in its infancy. Indeed, the studies of ion-beam processes in GaN reported in the literature have shown that this material exhibits quite unusual and rather complex behavior under ion bombardment. More work is needed before ion damage and its influence on structural, mechanical, optical, and electrical properties of GaN are fully understood. We hope that this review will attract interest and stimulate additional work on a number of technologically important (and, at the same time, physically-interesting) issues of the ion-beam processes in GaN discussed here.

Acknowledgements

We are grateful to a number of people involved in this work through collaboration and discussion, including C. Jagadish, J. Zou, G. Li, M. Toth, M.R. Phillips, J.E. Bradby, M.V. Swain, H. Boudinov, V.S.J. Craig, A.I. Titov, J.A. Davies, J.C. Zolper, C. Vartuli, X.A. Cao, F. Ren, C.R. Abernathy, R.G. Wilson, and J.M. Zavada. The work at UF is partially supported by NSF-DMR 972865 and by DARPA/EPRI MDA 972-1-0006.

References

[1] S.J. Pearton, J.C. Zolper, R.J. Shul, F. Ren, J. Appl. Phys. 86 (1999) 1 and references therein.
[2] J.C. Zolper, R.J. Shul, MRS Bull. 22 (1997) 36.
[3] J.C. Zolper, in: S.J. Pearton (Ed.), Gallium Nitride and Related Materials, Gordon and Breach, New York, 1997.
[4] J.S. Williams, Mater. Sci. Eng. A 253 (1998) 8.
[5] B. Rauschenbach, in: M. Manasreh (Ed.), III Nitride Semiconductors: Electrical, Structural and Defects Properties, Elsevier, 2000.
[6] C.R. Eddy Jr., B. Molnar, J. Electron. Mater. 28 (1999) 314.
[7] M. Nastasi, J.W. Mayer, J.K. Hirvonen, Ion–Solid Interactions: Fundamentals and Applications, Cambridge University Press, Cambridge, 1996.
[8] D.J. Mazey, R.S. Nelson, R.S. Barnes, Philos. Mag. 17 (1968) 1145.
[9] L.M. Howe, M.H. Rainville, Nucl. Instr. Meth. B. 19/20 (1987) 61.
[10] J.A. Davies, in: J.S. Williams, J.M. Poate (Eds.), Ion Implantation and Beam Processing, Academic Press, Sydney, 1984.
[11] J.P. Biersack, L.G. Haggmark, Nucl. Instr. 174 (1980) 257.
[12] J.F. Gibbons, L.A. Christel, in: J.S. Williams, J.M. Poate (Eds.), Ion Implantation and Beam Processing, Academic Press, Sydney, 1984.
[13] W.-K. Chu, J.W. Mayer, M.-A. Nicolet, Backscattering Spectrometry, Academic Press, Orlando, 1978.
[14] H.H. Tan, J.S. Williams, J. Zou, D.J. Cockayne, S.J. Pearton, R.A. Stall, Appl. Phys. Lett. 69 (1996) 2364.
[15] H.H. Tan, J.S. Williams, J. Zou, D.J. Cockayne, S.J. Pearton, C. Yuan, Electrochem. Soc. Proc. 96-11 (1996) 142.
[16] S. Strite, P.W. Epperlein, A. Dommann, A. Rockett, R.F. Broom, Mater. Res. Soc. Symp. Proc. 395 (1996) 795.
[17] N. Parikh, A. Suvkhanov, M. Lioubtchenko, E. Carlson, M. Bremser, D. Bray, R. Davis, J. Hunn, Nucl. Instr. Meth. B 127/128 (1997) 463.
[18] C. Liu, B. Mensching, K. Volz, B. Rauschenbach, Appl. Phys. Lett. 71 (1997) 2313.
[19] C. Ronning, M. Dalmer, M. Deicher, M. Restle, M.D. Bremser, R.F. Davis, H. Hofsass, Mater. Res. Soc. Symp. Proc. 468 (1997) 407.
[20] A. Suvkhanov, J. Hunn, W. Wu, D. Thomson, K. Price, N. Parikh, E. Irene, R.F. Davis, L. Krasnobaev, Mater. Res. Soc. Symp. Proc. 512 (1998) 475.
[21] H.H. Tan, J.S. Williams, J. Zou, D.J. Cockayne, S.J. Pearton, J.C. Zolper, R.A. Stall, Appl. Phys. Lett. 72 (1998) 1190.
[22] C. Liu, B. Mensching, M. Zeitler, K. Volz, B. Rauschenbach, Phys. Rev. B 57 (1998) 2530.
[23] B.J. Pong, C.J. Pan, Y.C. Teng, G.C. Chi, W.-H. Li, K.C. Lee, C.-H. Lee, J. Appl. Phys. 83 (1998) 5992.
[24] W. Jiang, W.J. Weber, S. Thevuthasan, G.J. Exarhos, B.J. Bozlee, MRS Internet J. Nitride Semicond. Res. 4S1 (1999) G6.15.

[25] W.R. Wampler, S.M. Myers, MRS Internet J. Nitride Semicond. Res. 4S1 (1999) G3.73.
[26] A. Wenzel, C. Liu, B. Rauschenbach, Mater. Sci. Eng. B 59 (1999) 191.
[27] C. Liu, A. Wenzel, K. Volz, B. Rauschenbach, Nucl. Instr. Meth. B 148 (1999) 396.
[28] S.O. Kucheyev, J.S. Williams, C. Jagadish, G. Li, S.J. Pearton, Appl. Phys. Lett. 76 (2000) 3899.
[29] W. Jiang, W.J. Weber, S. Thevuthasan, J. Appl. Phys. 87 (2000) 7671.
[30] S.O. Kucheyev, J.S. Williams, C. Jagadish, J. Zou, M. Toth, M.R. Phillips, H.H. Tan, G. Li, S.J. Pearton, Mater. Res. Soc. Symp. Proc. 622 (2000) T7.9.1.
[31] C. Liu, M. Schreck, A. Wenzel, B. Mensching, B. Rauschenbach, Appl. Phys. A 70 (2000) 53.
[32] S.O. Kucheyev, J.S. Williams, C. Jagadish, J. Zou, V.S.J. Craig, G. Li, Appl. Phys. Lett. 77 (2000) 1455.
[33] S.O. Kucheyev, J.S. Williams, C. Jagadish, J. Zou, G. Li, Phys. Rev. B 62 (2000) 7510.
[34] C. Ronning, M. Dalmer, M. Uhrmacher, M. Restle, U. Vetter, L. Ziegeler, T. Gehrke, K. Jarrendahl, R.F. Davis, ISOLDE Collaboration, J. Appl. Phys. 87 (2000) 2149.
[35] S.O. Kucheyev, J.S. Williams, J. Zou, C. Jagadish, G. Li, Nucl. Instrum. Methods Phys. Res. B, in press.
[36] S.O. Kucheyev, J.S. Williams, J. Zou, C. Jagadish, G. Li, Appl. Phys. Lett. 77 (2000) 3577.
[37] S.O. Kucheyev, J.S. Williams, J. Zou, C. Jagadish, G. Li, Appl. Phys. Lett. 78 (2001) 1373.
[38] S.O. Kucheyev, J.S. Williams, C. Jagadish, J. Zou, G. Li, J. Appl. Phys. 88 (2000) 5493.
[39] S.O. Kucheyev, J.S. Williams, J. Zou, C. Jagadish, G. Li, Nucl. Instr. Meth. B 175–177 (2001) 230.
[40] X.A. Cao, S.J. Pearton, A.P. Zhang, G.T. Dang, F. Ren, R.J. Shul, L. Zhang, R. Hickman, J.M. Van Hove, Appl. Phys. Lett. 75 (1999) 2569.
[41] J.F. Gibbons, Proc. IEEE 60 (1972) 1062.
[42] S.O. Kucheyev, J.S. Williams, unpublished.
[43] J.S. Williams, Trans. Mater. Res. Soc. Jpn. 17 (1994) 417.
[44] M.L. Swanson, J.R. Parsons, C.W. Hoelke, Radiat. Effect 9 (1971) 249.
[45] A.I. Titov, G. Carter, Nucl. Instrum. Methods Phys. Res. B 119 (1996) 491.
[46] W.J. Weber, Nucl. Instrum. Methods Phys. Res. B 166/167 (2000) 98.
[47] B.R. Appleton, O.W. Holland, J. Narayan, O.E. Schow III, J.S. Williams, K.T. Short, E. Lawson, Appl. Phys. Lett. 41 (1982) 711.
[48] L.M. Wang, R.C. Britcher, Philos. Mag. A 64 (1991) 1209 and references therein.
[49] G.L. Destefanis, J.P. Gailliard, Appl. Phys. Lett. 36 (1980) 40.
[50] R. Callec, P.N. Favennec, M. Salvi, H. L'Haridon, M. Gauneau, Appl. Phys. Lett. 59 (1991) 1872.
[51] T.K. Chaki, J.C.M. Li, Philos. Mag. B 51 (1985) 557.
[52] L.A. Christel, J.F. Gibbons, J. Appl. Phys. 52 (1981) 5050.
[53] H.H. Andersen, in: J.S. Williams, J.M. Poate (Eds.), Ion Implantation and Beam Processing, Academic Press, Sydney, 1984.
[54] F. Priolo, E. Rimini, Mater. Sci. Rep. 5 (1990) 319.
[55] T.Y. Tsui, G.M. Pharr, J. Mater. Res. 14 (1999) 292.
[56] M.D. Drory, J.W. Ager III, T. Suski, I. Grzegory, S. Porowski, Appl. Phys. Lett. 69 (1996) 4044.
[57] G. Yu, H. Ishikawa, T. Egawa, T. Soga, J. Watanabe, T. Jimbo, M. Umeno, J. Cryst. Growth 189/190 (1998) 701.
[58] Yonenaga, T. Hoshi, A. Usui, Mater. Res. Soc. Symp. Proc. 595 (1999) W3.90.1.
[59] R. Nowak, M. Pessa, M. Suganuma, M. Leszczynski, I. Grzegory, S. Porowski, F. Yoshida, Appl. Phys. Lett. 75 (1999) 2070.
[60] Cáceres, I. Vergara, R. González, E. Monroy, F. Calle, E. Munoz, F. Omnés, J. Appl. Phys. 86 (1999) 6773.
[61] M.H. Hong, A.V. Samant, V. Orlov, B. Farber, C. Kisielowski, P. Pirouz, Mater. Res. Soc. Symp. Proc. 572 (1999) 369.
[62] M.H. Hong, P. Pirouz, P.M. Tavernier, D.R. Clarke, Mater. Res. Soc. Symp. Proc. 622, 2000, T6.18.
[63] S.O. Kucheyev, J.E. Bradby, J.S. Williams, C. Jagadish, M. Toth, M.R. Phillips, M.V. Swain, Appl. Phys. Lett. 77 (2000) 3373.
[64] S.O. Kucheyev, J.E. Bradby, J.S. Williams, C. Jagadish, M.V. Swain, G. Li, Appl. Phys. Lett. 78 (2001) 156.
[65] J.S. Williams, Y. Chen, J. Wong-Leung, A. Kerr, M.V. Swain, J. Mater. Res. 14 (1999) 2338.
[66] J.E. Bradby, J.S. Williams, M.V. Swain, unpublished.
[67] J.A. Van Vechten, Phys. Rev. B 7 (1973) 1479.
[68] C. Ronning, H. Hofsass, A. Stoetzler, M. Deicher, E.P. Carlson, P.J. Hartlieb, T. Gehrke, P. Rajagopal, R.F. Davis, Mater. Res. Soc. Symp. Proc. 595 (2000) W11.44.1.
[69] C. Ronning, K.J. Linthicum, E.P. Carlson, P.J. Hartlieb, D.B. Thomson, T. Gehrke, R.F. Davis, MRS Internet J. Nitride Semicond. Res. 4S1 (1999) G3.17.
[70] C. Ronning, E.P. Carlson, D.B. Thomson, R.F. Davis, Appl. Phys. Lett. 73 (1998) 1622.
[71] E. Alves, M.F. DaSilva, J.C. Soares, J. Bartels, R. Vianden, C.R. Abernathy, S.J. Pearton, MRS Internet J. Nitride Semicond. Res. 4S1 (1999) G11.2.
[72] M. Dalmer, M. Restle, M. Sebastian, U. Vetter, H. Hofsass, M.D. Bremser, C. Ronning, R.F. Davis, U. Wahl, K. Bharuth-Ram, ISOLDE Collaboration, J. Appl. Phys. 84 (1998) 3085.

[73] H. Kobayashi, W.M. Gibson, Appl. Phys. Lett. 73 (1998) 1406.
[74] H. Kobayashi, W.M. Gibson, Appl. Phys. Lett. 74 (1999) 2355.
[75] U. Wahl, A. Vantomme, G. Langouche, J.P. Araujo, L. Peralta, J.G. Correia, ISOLDE Collaboration, J. Appl. Phys. 88 (2000) 1319.
[76] Burchard, E.E. Haller, A. Stoetzler, R. Weissenborn, M. Deicher, ISOLDE Collaboration, Phys. B 273/274 (1999) 96.
[77] W. Limmer, W. Ritter, R. Sauer, B. Mensching, C. Liu, B. Rauschenbach, Appl. Phys. Lett. 72 (1998) 2589.
[78] K. Lorenz, R. Vianden, S.J. Pearton, C.R. Abernathy, J.M. Zavada, MRS Internet J. Nitride Semicond. Res. 5 (2000) 5.
[79] J.I. Pankove, J.A. Hutchby, J. Appl. Phys. 47 (1976) 5387.
[80] J.I. Pankove, J.A. Hutchby, Appl. Phys. Lett. 24 (1974) 281.
[81] R.D. Metcalfe, D. Wickenden, W.C. Clark, J. Lum. 16 (1978) 405.
[82] I.Sh. Khasanov, A.V. Kuznetsov, A.A. Gippius, S.A. Semiletov, Sov. Phys. Semicond. 17 (1983) 187.
[83] E. Silkowski, Y.K. Yeo, R.L. Hengehold, M.A. Khan, T. Lei, K. Evans, C. Cerny, Mater. Res. Soc. Symp. Proc. 395 (1996) 813.
[84] J.C. Zolper, H.H. Tan, J.S. Williams, J. Zou, D.J.H. Cockayne, S.J. Pearton, M.H. Crawford, R.F. Karlicek Jr., Appl. Phys. Lett. 70 (1997) 2729.
[85] R. Zhang, L. Zhang, N. Perkins, T.F. Kuech, Mater. Res. Soc. Symp. Proc. 512 (1998) 321.
[86] T. Suski, J. Jun, M. Leszczynski, H. Teisseyre, S. Strite, A. Rockett, A. Pelzmann, M. Kamp, K.J. Ebeling, J. Appl. Phys. 84 (1998) 1155.
[87] C. Uzan-Saguy, J. Salzman, R. Kalish, V. Richter, U. Tish, S. Zamir, S. Prawer, Appl. Phys. Lett. 74 (1999) 2441.
[88] S.O. Kucheyev, J.S. Williams, C. Jagadish, J. Zou, M. Toth, M.R. Phillips, G. Li, in: Proceedings of 11th International Semiconducting and Insulating Materials Conference (SIMC-XI), EEE Publishing 001, p. 47.
[89] S.O. Kucheyev, J.S. Williams, J. Zou, J.E. Bradby, C. Jagadish, G. Li, Phys. Rev. Lett. 863 (2001) 113202.
[90] S.O. Kucheyev, M. Toth, M.R. Phillips, J.S. Williams, C. Jagadish, G. Li, Appl. Phys. Lett. 78 (2001) 34.
[91] J.C. Zolper, J. Han, R.M. Biefeld, S.B. Van Deusen, W.R. Wampler, D.J. Reiger, S.J. Pearton, J.S. Williams, H.H. Tan, R.A. Stall, J. Electron. Mater. 27 (1998) 179.
[92] R.G. Wilson, et al., J. Vac. Sci. Technol. A 17 (1999) 1226.
[93] R.G. Wilson, S.J. Pearton, C.R. Abernathy, J.M. Zavada, Appl. Phys. Lett. 66 (1995) 2238.
[94] J.C. Zolper, R.G. Wilson, S.J. Pearton, A. Stall, Appl. Phys. Lett. 68 (1996) 1945.
[95] X.A. Cao, C.R. Abernathy, R.K. Singh, S.J. Pearton, M. Fu, V. Sarvepalli, J.A. Sekhar, J.C. Zolper, D.J. Rieger, J. Han, T.J. Drummond, R.A. Stall, R.G. Wilson, Appl. Phys. Lett. 73 (1998) 229.
[96] R.G. Wilson, C.B. Vartuli, C.R. Abernathy, S.J. Pearton, J.M. Zavada, Solid State Electron. 38 (1995) 1329.
[97] E.V. Kalinina, V.V. Solov'ev, A.S. Zubrilov, V.A. Dmitriev, A.P. Kovarsky, MRS Internet J. Nitride Semicond. Res. 4S1 (1999) G6.53.
[98] M.D. Deal, H.G. Robinson, Appl. Phys. Lett. 55 (1989) 1990.
[99] H.G. Robinson, M.D. Deal, D.A. Stevenson, Appl. Phys. Lett. 58 (1991) 2000.
[100] M.D. Deal, C.J. Hu, C.C. Lee, H.G. Robinson, Mater. Res. Soc. Symp. Proc. 300 (1993) 365.
[101] S.J. Pearton, C.R. Abernathy, Appl. Phys. Lett. 55 (1989) 678.
[102] H.G. Robinson, M.D. Deal, P.B. Griffin, G. Amaratunga, D.A. Stevenson, J.D. Plummer, J. Appl. Phys. 71 (1992) 2615.
[103] M.S. Feng, J.D. Guo, G.C. Chi, Proc. Electrochem. Soc. 95-21 (1995) 43.
[104] A.Y. Polyakov, M. Shin, M. Skowronski, R.G. Wilson, D.W. Greve, S.J. Pearton, Solid-State Electron. 41 (1997) 703.
[105] M. Dalmer, M. Restle, U. Vetter, H. Hofsass, M.D. Bremser, C. Ronning, R.F. Davis, ISOLDE Collaboration, Mater. Res. Soc. Symp. Proc. 482 (1998) 1021.
[106] V.A. Joshkin, C.A. Parker, S.M. Bedair, L.Y. Krasnobaev, J.J. Cuomo, R.F. Davis, A. Suvkhanov, Appl. Phys. Lett. 72 (1998) 2838.
[107] S. Fischer, G. Stewed, D.M. Hofmann, F. Kurth, F. Anders, M. Topf, B.K. Meyer, F. Bertram, M. Schmidt, J. Christen, L. Eckey, J. Holst, A. Hoffmenn, B. Mensching, B. Rauschenbach, J. Cryst. Growth 189/190 (1998) 556.
[108] M.G. Weinstein, M. Stavola, C.Y. Song, C. Bozdog, H. Przbylinska, G.D. Watkins, S.J. Pearton, R.G. Wilson, MRS Internet J. Nitride Semicond. Res. 4S1 (1999) G5.9.
[109] H.W. Kunert, S. Juillaguet, J. Camassel, J.B. Malherbe, R.Q. Odendaal, D.J. Brink, L.C. Prinsloo, Phys. Stat. Sol. (b) 216 (1999) 619.
[110] Kaufmann, A. Dörnen, V. Härle, H. Bolay, F. Scholz, G. Pensl, Appl. Phys. Lett. 68 (1996) 203.
[111] J.W. Orton, C.T. Foxon, Rep. Prog. Phys. 61 (1998) 1.
[112] A. Billeb, W. Grieshaber, D. Stocker, E.F. Schubert, R.F. Karlicek Jr., Appl. Phys. Lett. 70 (1997) 2790.
[113] K. Kanaya, S. Okayama, J. Phys. D 5 (1972) 43.
[114] K. Fleischer, M. Toth, M.R. Phillips, J. Zou, G. Li, S.J. Chua, Appl. Phys. Lett. 74 (1999) 1114.
[115] S.O. Kucheyev, M. Toth, M.R. Phillips, J.S. Williams, C. Jagadish, G. Li, unpublished.
[116] T. Ogino, M. Aoki, Jpn. J. Appl. Phys. 19 (1980) 2395.

[117] M. Toth, K. Fleshier, M.R. Phillips, Phys. Rev. B 59 (1999) 1575.
[118] M. Linde, S.J. Uftring, G.D. Watkins, V. Härle, F. Scholz, Phys. Rev. B 55 (1997) R10177.
[119] I.A. Buyanova, Mt. Wagner, W.M. Chen, B. Monemar, J.L. Lindstrom, H. Amano, I. Akasaki, Appl. Phys. Lett. 73 (1998) 2968.
[120] C. Bozdog, H. Przbylinska, G.D. Watkins, V. Härle, F. Scholz, M. Mayer, M. Kamp, R.J. Molnar, A.E. Wickenden, D.D. Koleske, R.L. Henry, Phys. Rev. B 59 (1999) 12479.
[121] S.J. Pearton, C.B. Vartuli, J.C. Zolper, C. Yuan, R.A. Stall, Appl. Phys. Lett. 67 (1995) 1435.
[122] J.C. Zolper, D.J. Reiger, A.G. Baca, S.J. Pearton, J.W. Lee, R.A. Stall, Appl. Phys. Lett. 69 (1996) 538.
[123] M. Fu, V. Sarvepalli, R.K. Singh, C.R. Abernathy, X.A. Cao, S.J. Pearton, J.A. Sekhar, Mater. Res. Soc. Symp. Proc. 483 (1998) 345.
[124] C.C. Yi, B.W. Wessels, Appl. Phys. Lett. 69 (1996) 3206.
[125] H.H. Tan, C. Jagadish, J.S. Williams, H. Zoa, D.J.H. Cockayne, A. Sikorski, J. Appl. Phys. 77 (1995) 87.
[126] J.C. Zolper, J. Han, S.B. Van Deusen, R. Biefeld, M.H. Crawford, J. Jun, T. Suski, J.M. Baranowski, S.J. Pearton, Mater. Res. Soc. Symp. 482 (1998) 618.
[127] P. Bogulawski, E.L. Briggs, J. Bernholc, Phys. Rev. B 51 (1995) 17255.
[128] C.R. Abernathy, J.D. MacKenzie, S.J. Pearton, W.S. Hobson, Appl. Phys. Lett. 66 (1995) 1969.
[129] B. Mensching, C. Liu, B. Rauschenbach, K. Kornitzer, W. Ritter, Mater. Sci. Eng. B 50 (1997) 105.
[130] J.S. Chan, N.W. Cheung, L. Schloss, E. Hones, W.S. Wong, N. Newman, X. Liu, R.R. Weber, A. Gassman, M.D. Rubin, Appl. Phys. Lett. 68 (1996) 2702.
[131] A. Pelzmann, S. Strite, A. Dommann, C. Kirchner, M. Kamp, K.J. Ebeling, A. Nazzal, MRS Internet J. Nitride Semicond. Res. 2 (1997) 4.
[132] S. Strite, A. Pelzmann, T. Suski, M. Leszczynski, J. Jun, A. Rockett, M. Kamp, K.J. Ebling, MRS Internet J. Nitride Semicond. Res. 2 (1997) 15.
[133] F. Bernardini, V. Fiorentini, A. Bosin, Appl. Phys. Lett. 70 (1997) 2990.
[134] O. Brandt, H. Yang, H. Kostial, K. Ploog, Appl. Phys. Lett. 69 (1996) 2707.
[135] F.D. Auret, S.A. Goodman, F.K. Koschnick, J.-M. Spaeth, B. Beaumont, P. Gibart, Appl. Phys. Lett. 73 (1998) 3745.
[136] F.D. Auret, S.A. Goodman, F.K. Koschnick, J.-M. Spaeth, B. Beaumont, P. Gibart, Appl. Phys. Lett. 73 (1998) 407.
[137] S.A. Goodman, F.D. Auret, F.K. Koschnick, J.-M. Spaeth, B. Beaumont, P. Gibart, Appl. Phys. Lett. 74 (1999) 809.
[138] F.D. Auret, S.A. Goodman, F.K. Koschnick, J.-M. Spaeth, B. Beaumont, P. Gibart, Appl. Phys. Lett. 73 (1998) 2173.
[139] F.D. Auret, W.E. Meyer, S.A. Goodman, F.K. Koschnick, J.-M. Spaeth, B. Beaumont, P. Gibart, Phys. B 273/274 (1999) 92.
[140] F.D. Auret, W.E. Meyer, S.A. Goodman, F.K. Koschnick, J.-M. Spaeth, B. Beaumont, P. Gibart, Phys. B. 273/274 (1999) 84.
[141] D. Hasse, M. Schmidt, W. Kurner, A. Dornen, V. Harle, F. Scholz, M. Burkard, H. Schweizer, Appl. Phys. Lett. 69 (1996) 2525.
[142] D.C. Look, D.C. Reynolds, J.W. Hemsky, J.R. Sizelove, R.L. Jones, R.J. Molnar, Phys. Rev. Lett. 79 (1997) 2273.
[143] Z.-Q. Fang, J.W. Hemsky, D.C. Look, M.P. Mack, Appl. Phys. Lett. 72 (1998) 448.
[144] L. Polenta, Z.-Q. Fang, D.C. Look, Appl. Phys. Lett. 76 (2000) 2086.
[145] V.V. Emtsev, V. Yu, Davydov, C.C. Kozlovskii, D.S. Polskin, A.N. Smirnov, N.M. Shmidt, A.S. Usikov, Phys. B 273/274 (1999) 101.
[146] K.H. Chow, G.D. Watkins, A. Usui, M. Mizuta, Phys. Rev. Lett. 85 (2000) 2761.
[147] S.J. Pearton, Mater. Sci. Rep. 4 (1990) 313.
[148] M. Orenstein, N.G. Stoffel, A.C. Von Lehmen, J.P. Harbison, L.T. Florez, Appl. Phys. Lett. 59 (1991) 31.
[149] K.L. Lear, R.P. Schneider, K.D. Choquette, S.P. Kilcoyne, J.J. Figiel, J.C. Zolper, IEEE Photonic Tech. Lett. 6 (1994) 1053.
[150] J.C. Zolper, A.G. Baca, S.A. Chalmers, Appl. Phys. Lett. 62 (1993) 2536.
[151] S.J. Pearton, M.P. Iannuzzi, C.L. Reynolds Jr., L. Peticolas, Appl. Phys. Lett. 52 (1988) 395.
[152] J.C. Zolper, M.E. Sherwin, A.G. Baca, R.P. Schneider Jr., J. Electron. Mater. 24 (1995) 21.
[153] S.C. Binari, H.B. Dietrich, G. Kelner, L.B. Rowland, K. Doverspike, D.K. Wickenden, J. Appl. Phys. 78 (1995) 3008.
[154] S.J. Pearton, R.G. Wilson, J.M. Zavada, J. Han, R.J. Shul, Appl. Phys. Lett. 73 (1998) 1877.
[155] M. Hayes, S.A. Goodman, F.D. Auret, Nucl. Instrum. Methods Phys. Res. B 148 (1999) 437.
[156] X.A. Cao, S.J. Pearton, G.T. Dang, A.P. Zhang, F. Ren, R.G. Wilson, J.M. Van Hove, J. Appl. Phys. 87 (2000) 1091.
[157] H. Boudinov, S.O. Kucheyev, J.S. Williams, C. Jagadish, Appl. Phys. Lett. 78 (2001) 943.
[158] G. Harrington, Y. Hsin, Q.Z. Liu, P.M. Asbeck, S.S. Lau, M.A. Khan, J.W. Yang, Q. Chen, Electron. Lett. 34 (1998) 193.
[159] X.A. Cao, F. Ren, S.J. Pearton, A. Zeitouny, M. Eizenberg, J.C. Zolper, C.R. Abernathy, J. Han, R.J. Shul, J.R. Lothian, J. Vac. Sci. Technol. A 17 (1999) 1221 .